Journal of Geophysical Research Earth Surface

Supporting Information for

Quantifying near-surface rock strength on a regional scale from hillslope stability models

K.F. Townsend[1], S.F. Gallen[2†], M.K. Clark[1]

[1]Department of Earth and Environmental Sciences, University of Michigan, Ann Arbor, MI, USA, [2]Department of Earth Sciences, ETH Zürich, Switzerland, [†]Present Address: Department of Geosciences, Colorado State University, Fort Collins, CO, USA

Contents of this file

Additional Supporting Information (Files uploaded separately)

Townsend_ds02.zip. Contains a file geodatabase with remapped polygons for landslides produced during the 1994 M_w 6.7 Northridge Earthquake.

Introduction

This supplemental document contains a summary of laboratory and analytical protocols for analysis of apatite (U-Th)/He thermochronometry, landslide mapping methods, Culmann model landslide thickness calculations, and a discussion of model misfit.

Text S1: Apatite (U-Th)/He Methods

Bedrock samples for (U-Th)/He low-temperature thermochronometry were collected in April 2016 to infer magnitudes of exhumation. Samples were crushed, sieved, and separated using standard methods to isolate apatite by exploiting differences in density and magnetic susceptibility. Individual mineral grains were hand-selected under a high-powered binocular microscope to screen for clarity, crystal morphology, and minimal inclusions of other potentially radiogenic minerals. Grains selected

for analysis were measured along major and minor axes, photographed, packaged into individual Pt tubes, and analyzed for ^{4}He content using an Australian Scientific Instruments Helium Instrument (Alphachron) at the University of Michigan Thermochronology Laboratory. Grains were heated for 5 minutes at 900°C, released ^{4}He was spiked with ^{3}He, and the ^{4}He /^{3}He ratio was measured on a Pfeiffer quadrupole mass spectrometer to determine the quantity of ^{4}He. Following this initial ^{4}He measurement, these analytical procedures were repeated to check for any additional extraction of ^{4}He that might be indicative of micro-inclusions of high-temperature radiogenic minerals that were not observed optically during grain selection. The Durango apatite age standard was also analyzed with our samples to ensure accuracy of measurements of unknown age. After measurement of ^{4}He, grains were dissolved and analyzed for U, Th and Sm concentrations following standard procedures (Reiners and Nicolescu, 2006) using a Thermo Scientific Elements 2 ICP-MS at the University of Arizona Radiogenic Helium Dating Laboratory.

Individual grain dates were solved for numerically in Matlab using parent and daughter nuclide concentrations and the age equation. Analytical uncertainties were propagated through the age equation using Monte Carlo methods. Grains with low uranium concentrations are particularly susceptible to age biases that result from uranium-implantation from surrounding U-rich phases (Spiegel et al., 2009). Grains with uranium concentrations under 5 ppm are reported but excluded from calculation of mean values. Outliers were identified following the Dean-Dixon method (Dean and Dixon, 1951) based on the 90 percent confidence interval at two significant digits. We applied this outlier test only to bedrock samples with a 2-sigma standard error greater than 15 percent of the mean age. Using the remaining grain ages, we calculated a mean apatite (U-Th)/He age for each sample (Table S1). Because the observed variability in our (U-Th)/He ages for individual bedrock samples is larger than the analytical error for single grains, we report mean ages for bedrock samples with uncertainty as the standard error of the mean for the multiple grains analyzed (reported as two-sigma uncertainty in Table S1). We consider bedrock samples that have a one-sigma standard deviation greater than 45 percent of the mean age to have low reproducibility, and we do not report a mean age for 16-PC-1 for this reason. Each replicate age of 16-PC-3 is as older or older than the middle- to late-Miocene depositional age of the Monterey Formation, indicating that the ages are inherited and do not reflect cooling of the sample. We therefore do not report a mean age here.

We examined our data to identify any existing grainsize-age or eU-age trends for individual bedrock samples. Grainsize-age trends may indicate the effect of crystal size on closure temperature (Reiners and Farley, 2001), whereas trends between effective uranium (eU) and age may reflect the effects of radiation damage on helium diffusion (Flowers et al., 2009; Guenthner et al., 2013). We do not observe significant grainsize-age trends in our data, but we do observe a positive eU-age trend in 16-PC-04. Excluding the outlier, this trend falls within the typical age variability expected from bedrock samples. However, the eU-age trend may also indicate radiation damage. Regardless, helium ages from this sample indicate that it was buried deeply enough to be thermally reset, which is sufficient for the argument presented in this manuscript.

Text S2: Landslide Inventory Remapping Methods

Landslides were identified in Google Earth using aerial imagery from May 1994. Where 1994 Google Earth imagery was unavailable, we referenced the original ~1:60,000 scale IRIS II photo strips used by Harp and Jibson (1995, 1996), which were acquired by the United States Air Force on January

17, 1994. We used a stereoscope, 10X magnification, and 20X magnification loupes to identify landslides on the physical image strips, and matched these areas to equivalent topography in Google Earth to map a 3D polygon. The IRIS photo strips were also used to spot-check regions of particularly concentrated landsliding where remapping in Google Earth proved challenging.

In photographic or satellite images, landslides are typically recognized by changes in appearance due to surface disturbance (increased albedo and surface roughness) and loss of vegetative cover. However, in areas of dense landsliding where adjacent slopes simultaneously fail, it can be challenging to determine unique polygon areas that define individual landslides. In these cases, we define the lateral margins using intact vegetation. Linear downslope sections of vegetation likely separated flow paths and were mapped as stable margins to adjacent landslides. Disturbed regions typically project to ridgetops, which we interpreted to be landslide source areas. Occasionally, individual source areas were recognized by scarps on ridge tops. Morphologic features were commonly difficult to identify in the 1994 imagery, so landslide toes were mapped as the furthest downslope extent of disturbance. We chose to remove landslide polygons in our remapping where the apparent density of disturbed area was less than the area of vegetative cover. We shifted landslide polygon locations if they were offset from the area of disturbance as inferred from the imagery. We also recognized additional disturbed areas in the imagery that were not originally outlined as landslides. As the USGS conducted field surveys in tandem with their original mapping effort, we chose to only outline landslides that the USGS had originally included within a landslide polygon.

Digital topography was also used to separate individual landslides by identifying minor ridges. Branching landslide polygons indicating multiple source areas and overlapping deposits were remapped by separating each source area and assigning the deposit to the largest. Where similarly sized landslides originated from distinct slopes and coalesced in a valley bottom, the deposits were divided equally and mapped with the respective sources (Figure 4B). Less frequently, USGS polygons with a single source contained multiple branched runout areas. If individual source areas could not be identified for each runout, only the largest runout area was outlined with the source. Within landslide polygons covering cliff bands, individual source areas could either be identified with the 1994 imagery or recognized based on the position of subtle ridges. Margins of the sources were outlined and projected downslope into the overlapping deposits to assign the portion of the deposit immediately below each source to the corresponding source area.

Text S3: Culmann Model Landslide Thickness Calculations

Landslides produced by the M_w 6.7 Northridge Earthquake predominately occurred as planar failures with thicknesses of 1 to 5 m (Harp and Jibson, 1996). Here we describe how landslide thickness predictions from the Culmann model are calculated. Newmark model landslide thickness calculation methods are in the main manuscript text and Gallen et al., (2015).

The derivation of the Culmann equation yields the following expression:

$$\theta = \frac{\beta+\phi}{2} \quad (1)$$

wherein the angle of the landslide failure plane (θ) is equal to the geometric mean of the average hillslope gradient (β) and the angle of internal friction (ϕ) (Figure S1). Equation 1 yields landslide failure

surfaces that are steeper than the hillslope gradient for hillslope segments with β less than ϕ, suggesting that the Culmann model is not capable of modeling landslides for shallow slopes. This is consistent with previous findings (Lu and Godt, 2013), so we restrict our calculation to hillslope segments with $\beta \geq \phi$. Using the basin-averaged ϕ, we calculate Θ of theoretical landslide failures for hillslope segments within each basin. The Culmann model predicts landslides with a wedge-shaped geometry (Figure S1), so we use Θ, β, and the critically-stable hillslope height (H_c) to calculate the change in length across the top of the landslide wedge (ΔL) with the following expression:

$$\Delta L = \frac{H_c}{\tan(\theta)} - \frac{H_c}{\tan(\beta)} \quad (2)$$

The maximum thickness of the landslide, t_{max} is then:

$$t_{max} = \sin(\theta) * \Delta L \quad (3)$$

Dividing t_{max} by two yields the average thickness of each landslide. The mean model thickness of all landslides estimated from measured hillslope segments in all 24 measurement regions is 1.4 m, and mean model landslide thickness of hillslopes segments within each measurement region are listed in Table S3. Despite the Culmann model's wedge-shaped approximation of landslide geometry, this mean value falls within the range of actual landslide thicknesses.

In applying the Culmann model to digital topography, we assume that hillslope segments that define the threshold in H vs. β represent the strength-limited portions of the landscape. Therefore, we expect that these hillslopes would be the most likely to fail in a landslide. We explore the theoretical distribution of landslide thicknesses sourced from only threshold hillslope segments. For constant material strength, we calculate H_c in increments of 0.1° of β between ϕ and 90° to produce a distribution of threshold hillslope segments. We then calculate theoretical landslide thicknesses in the same manner as described above for actual hillslope segments. The mean model thickness of all landslides estimated from theoretical critically-stable hillslope segments is 3.7 m, and mean model landslide thickness of critical hillslope segments within each measurement region are listed in Table S3. Mean landslide thicknesses of threshold hillslope segments are thicker than landslide thicknesses estimated by the measured hillslope geometries in each basin. This is expected given the wedge-shaped geometry of landslides modeled by the Culmann equation; threshold segments represent the tallest and steepest components of the landscape, and the greater mean difference between β and Θ in threshold data results in higher ΔL and t_{max}. Importantly, the mean values of landslide thickness from threshold hillslope segments is within the range of actual landslide thickness produced during the M_w 6.7 Northridge Earthquake.

Text S4: Synthetic Landslide Geometries for the Newmark Approach

Following Gallen et al. (2015), we use a set of geometric rules to calculate the location and 3D volume of each landslide. From each cell identified as a landslide failure point by the simplified Newmark model (Jibson, 2007), Equation 4 projects a failure plane upslope from a point at depth assuming the slope of the failure plane to be equal to the topographic gradient of the failure grid cell (Figure S30):

$$z_{fp} = z_f + d_{fp} \tan[S_{fp}] \quad (4)$$

Where z_{fp} is the elevation of each grid cell on the failure plane, z_f is the elevation of the Newmark failure cell, d_{fp} is the distance of each cell on the failure plane from the Newmark failure cell, and S_{fp} is the topographic slope of the Newmark failure cell. Next, the model calculates the maximum slope, S_m, of the topography above the failure plane using the maximum relief of the potential failure mass and distance between this point and the failure cell (Figure S30). If S_m is greater than S_{fp}, which only occurs for ~0.5 – 3% of modeled landslides, the model will progressively curve the failure plane to reduce the landslide thickness while preserving its plan view area using Equation 5:

$$z_{fp} = z_f + d_{fp} \tan\left[S_{fp} + d_{fp}\left(\frac{S_m - S_{fp}}{max(d_{fp})}\right)\right] \quad (5)$$

Equation 5 acts to progressively curve the failure plane from the gradient of the Newmark failure cell to a maximum angle set by the maximum slope (S_m) of failure mass above the plane defined by Equation 4 (Figure S30). The plan-view area of each landslide is defined with a searching algorithm that sequentially finds the three steepest neighboring grid cells upslope of the landslide failure cell until the failure plan daylights. For any given pixel, if the elevation of the topography exceeds the elevation of the projected failure plane, it is included as part of the landslide area. If the elevation of the projected landslide failure plane exceeds the elevation of the topography, the cell is removed from the landslide area.

This simple geometric approximation applied to digital topography produces synthetic landslide distributions that closely match observed power-law scaling of landslide frequency-area statistical distributions (Gallen et al., 2015). We note that this approach produces power law landslide frequency-area distributions for intermediate to large landslides, but cannot reproduce the rollover at small landslide areas seen in most mapped distributions, as a 1D approximation to slope stability does not censor short slopes where the driving stress is diminished compared to longer slopes.

Text S5: Quality of Model Fits to Data

We note variability in the quality of both Newmark synthetic landslide frequency-area fits to observed distributions, and the 'threshold' of hillslopes in height vs. gradient space (Figures S5 to S29). In this section we discuss reasons for the misfit and variability in agreement of the two models.

The variable quality of fits in the Newmark approach is mostly driven by a mismatch between the portions of the landscape that are predicted to fail by the simplified Newmark analysis of Jibson (2007), and the portions of the landscape that actually failed during the Northridge earthquake. The approach as adapted here is most sensitive to the number of landslides in each basin, but the

distribution of landslide areas within that number of landslides is determined by the topography where the Newmark model predicts landslide failures. In log-transformed frequency-area space, our model approach only changes the y-intercept of the power-law distribution, but not the slope of that relationship, which is a function of the topography within which the simplified Newmark model predicts failure cells. The poor fit to data in some catchments (e.g. catchments 1 and 21) suggests that the simplified Newmark model is predicting failures on topography that is dissimilar to what actually failed. We note that applying a scar correction to reduce landslide polygon areas does not improve the quality of fits. The size of landslides we can model is controlled by the resolution of the DEM, and despite the relatively high resolution (3m) of the DEM used here, reducing landslide polygon sizes severely reduces the number of landslides modeled. As we are fitting the total number of landslides in each basin, and the slope of the log-transformed line in frequency-area space is controlled by the topography where the landslides fail, reducing the number of landslides does not change the quality of the fits, but instead bias the results towards higher strength.

For the Culmann analysis, the threshold of hillslope data in height versus gradient space is variably well defined, with some regions yielding data with a larger number of tall moderately steep hillslopes than anticipated by a Culmann model. The approach taken here assumes that the strength of shallow bedrock underlying every hillslope in each basin is the same, but we recognize that in real landscapes, rock strength can be a function of many local variables, including topographic position, groundwater and hydrology, aspect, etc., that will produce local variability in strength that influence the local morphology of any individual hillslope. Further, the approach assumes topographic steady-state, but in reality, most landscapes will contain transient features (e.g. landslide head scarps) that may push a hillslope towards a steeper or shallower gradient than is average for the landscape. Results presented here represent an approximation of the average strength of shallow bedrock underlying hillslopes within each basin. Hillslope segments that fall along the threshold are distributed broadly across each catchment, which lends confidence to the interpretation of average strength.

The basins with poor Newmark fits are not systematically the basins that yield poorly-defined thresholds in hillslope height vs. gradient for the Culmann strength interpretations, and basins with large disagreement in cohesion do not necessarily exhibit poor model fits. For example, Basin 1 yields a poor fit between Newmark predicted and observed landslide frequency-area statistics, but the threshold in height vs. gradient space for the Culmann analysis is moderately well-defined. In contrast, basin 15 yields a close fit between Newmark predicted and observed frequency-area statistics, but the threshold in height vs. gradient space for the Culmann is diffuse and poorly-defined. The mismatch between model cohesion is noticeable in Basin 9 (Culmann C = 50 kPa, Newmark C = 6 kPa), which appears as an outlier in Figure 7B and 8. However, the synthetic Newmark landslide distribution closely fits the mapped distribution, and the threshold in height vs. gradient space is well defined for the Newmark model (Figure S13). A possible source of this disagreement is the assumption of strength-limited hillslopes for the Culmann analysis. We note the distribution of the tallest hillslopes is at a lower gradient (~30°) in basin 9 than for most basins underlain by the Pico Formation (~35-45°), but the width of this region is constrained by the San Cayetano fault to the south and the Piru Creek valley to the north. There may not be enough space for hillslopes over the entire distribution of gradients to reach lengths at which they become unstable. Approximating the threshold including these relatively low-gradient, tall hillslopes in height vs. gradient space with the Culmann model requires an anomalously low friction angle, yielding the high cohesion estimate. If hillslopes at ~35-45° are not strength-limited, and additional height is required before these hillslopes become unstable, then the distribution of hillslope data would yield a Culmann threshold with lower cohesion and higher friction, which would be more consistent with other basins overlying the Pico fm.

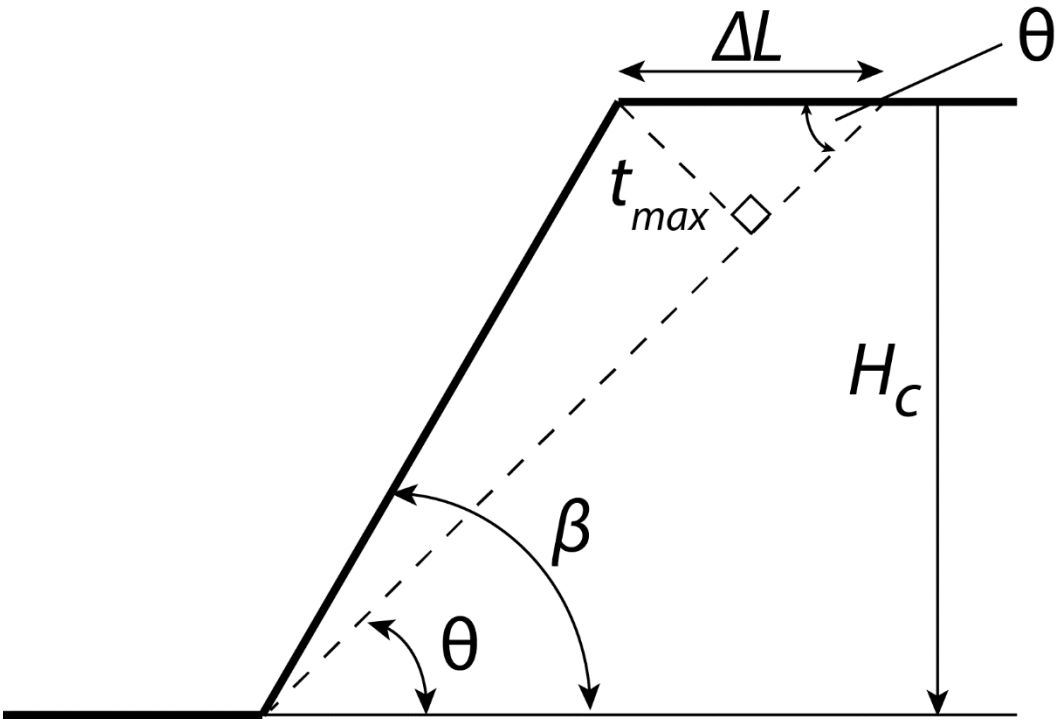

Figure S1. Illustration of the Culmann approximation of hillslope geometry and landslide thickness.

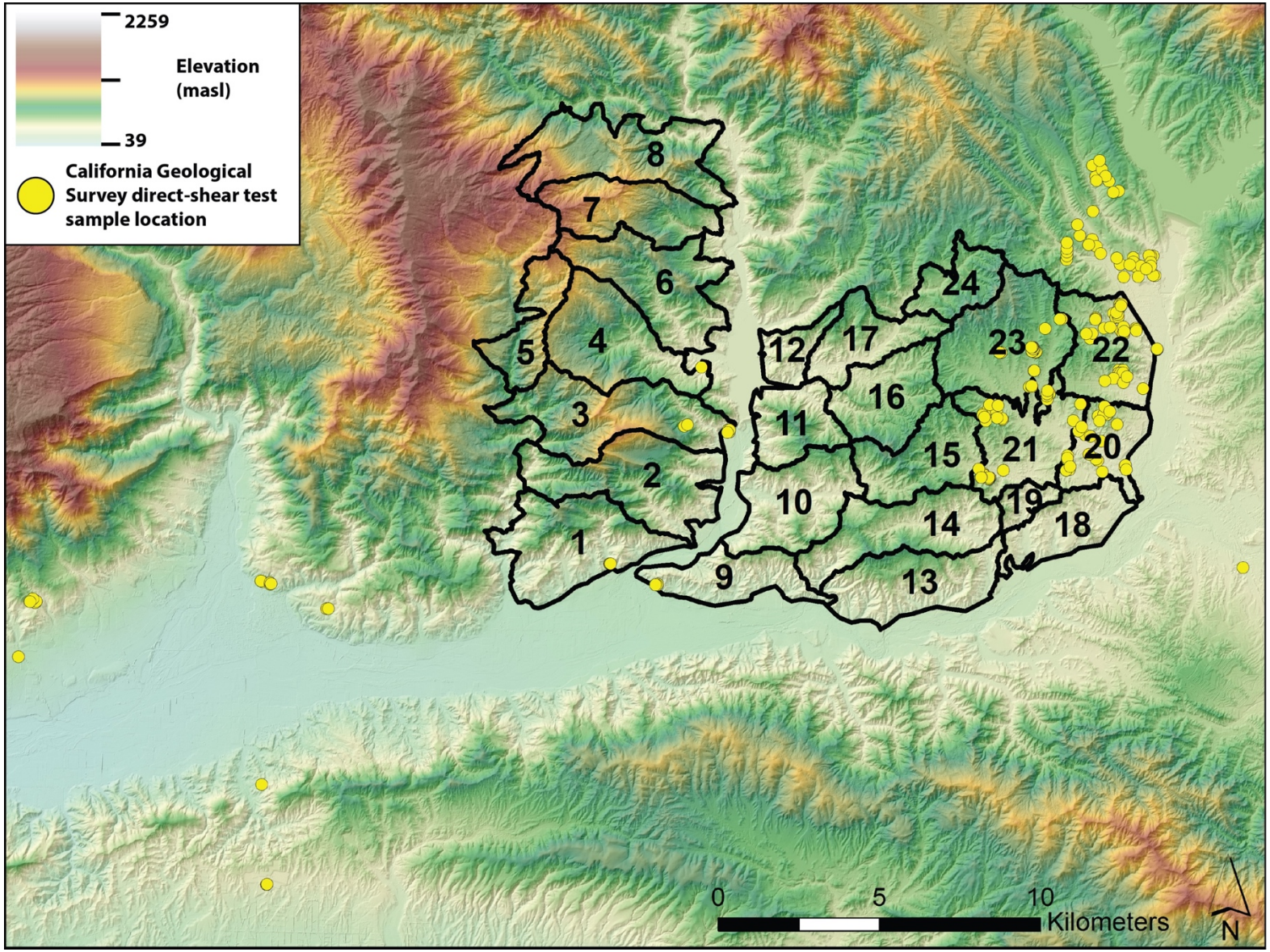

Figure S2. California Geological Survey sample locations for direct-shear testing used to produce mean estimates reported in Table 1.

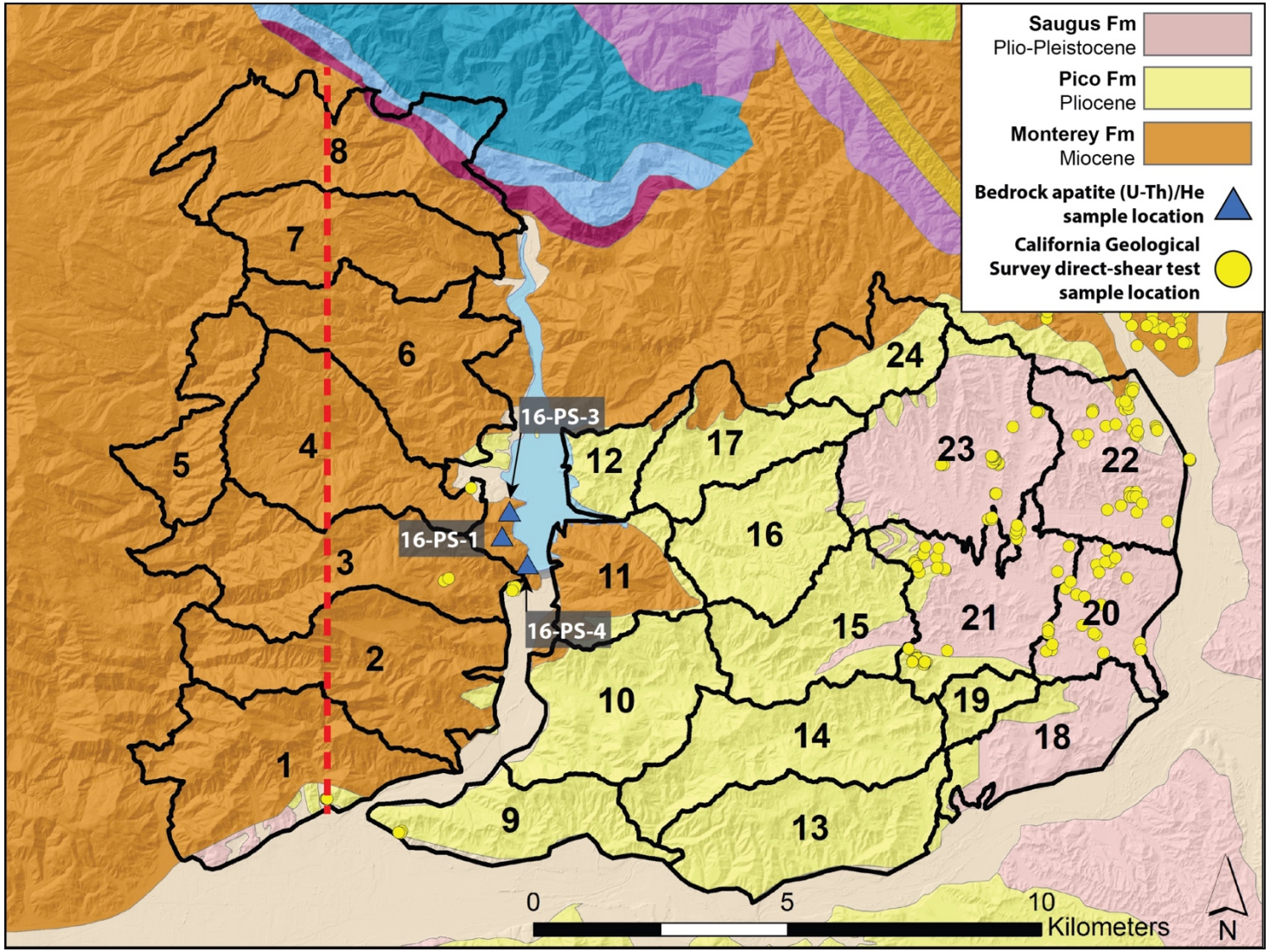

Figure S3. Topatopa basin numbers overlying mapped bedrock geology. Adapted from Dibblee (1991, 1993) and Dibblee and Ehrenspeck, (1996, 1997). Bedrock apatite (U-Th)/He thermochronology sample locations and California Geological Survey sample locations for direct-shear testing are shown. Red dashed line is the location of the geologic cross section and strength transects shown in Figure 8.

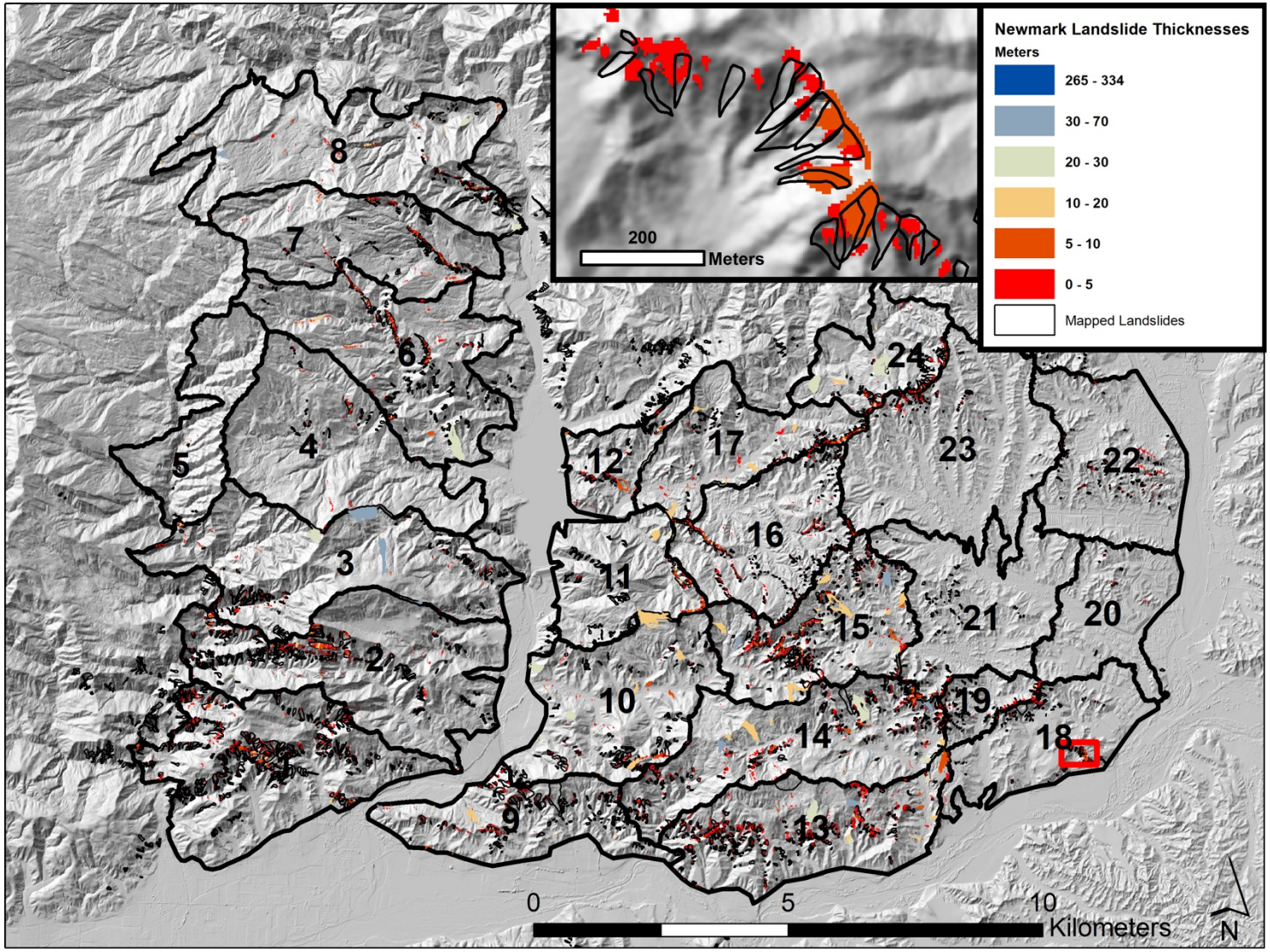

Figure S4. Distribution of synthetic landslides (n = 6185) produced using the Newmark approach, and landslides from the remapped inventory presented in this manuscript. Landslides are colored by modeled thickness. 92% of landslides are < 10 meters thick. Eight outlier landslides have thicknesses of 265-333 meters, but these are limited in spatial extent (maximum area of 325 square meters). Inset map shows close-up example of agreement between synthetic and mapped landslides from Basin 18 (red outline).

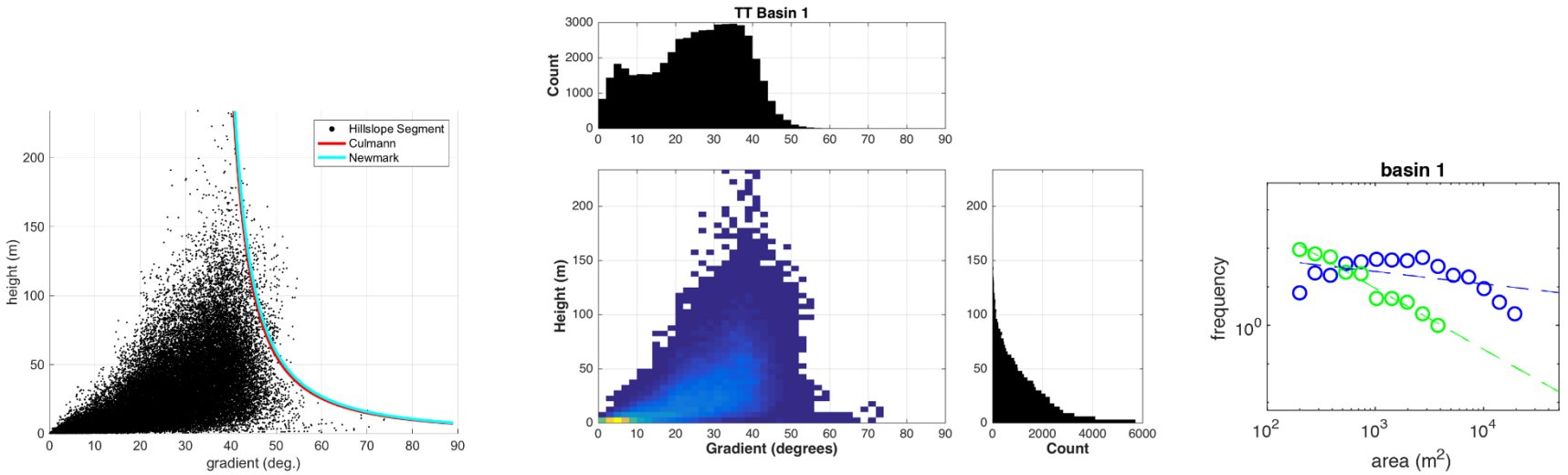

Figure S5. (left) Basin 1 hillslope gradient-height scatter plot with Culmann and Newmark curves, (center) hillslope gradient-height density plot and histograms, (right) frequency-area plots of mapped (blue) and synthetic (green) landslide distributions.

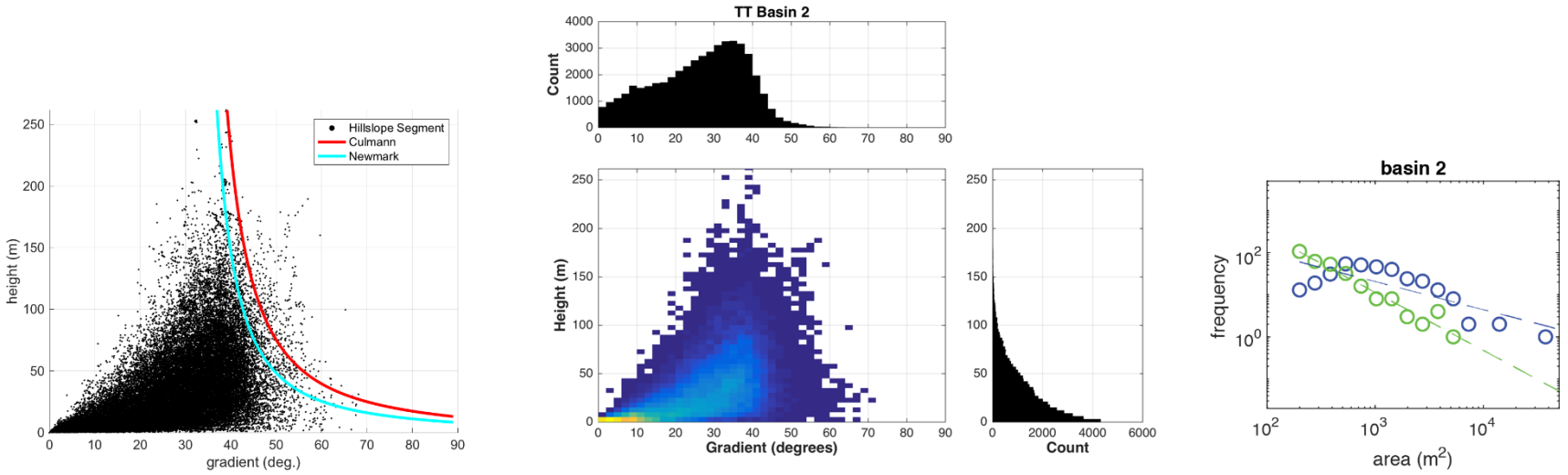

Figure S6. (left) Basin 2 hillslope gradient-height scatter plot with Culmann and Newmark curves, (center) hillslope gradient-height density plot and histograms, (right) frequency-area plots of mapped (blue) and synthetic (green) landslide distributions.

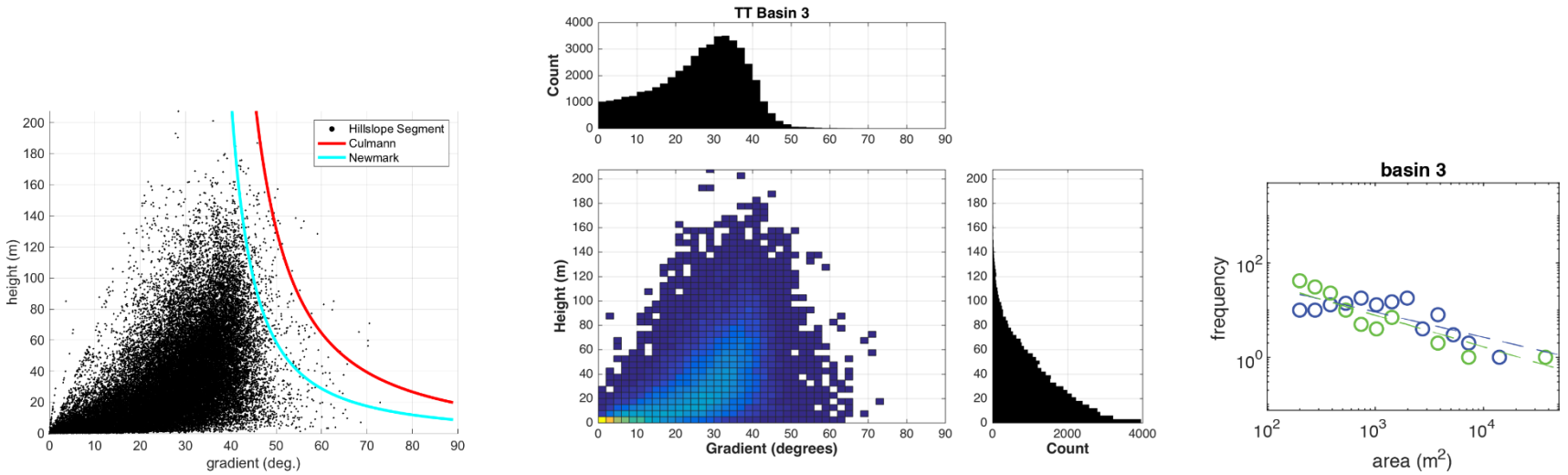

Figure S7. (left) Basin 3 hillslope gradient-height scatter plot with Culmann and Newmark curves, (center) hillslope gradient-height density plot and histograms, (right) frequency-area plots of mapped (blue) and synthetic (green) landslide distributions.

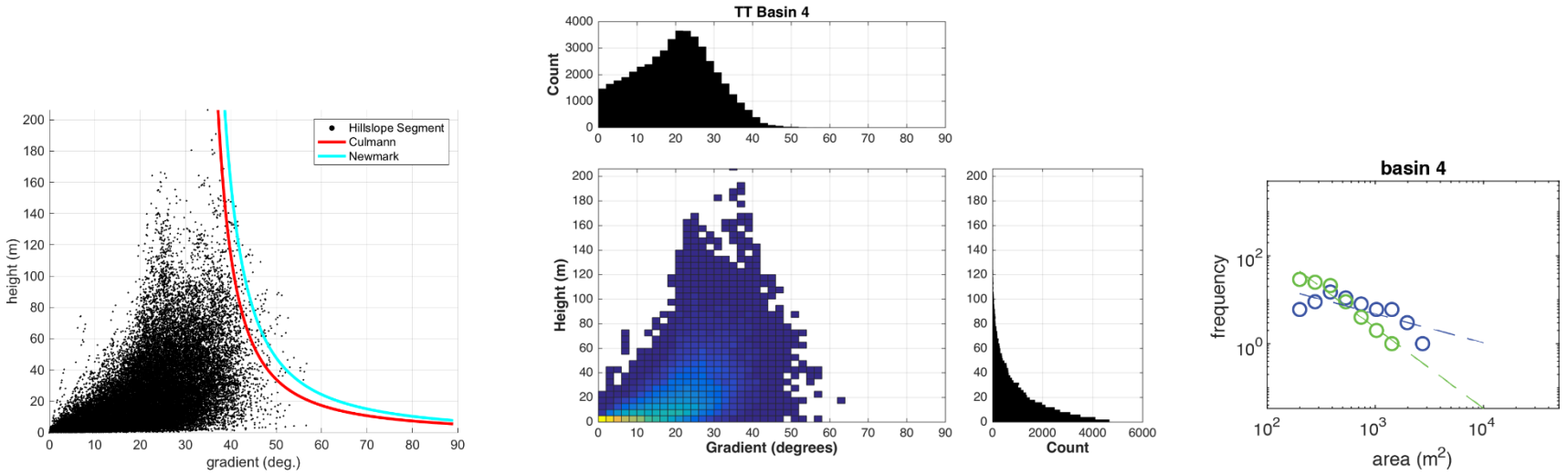

Figure S8. (left) Basin 4 hillslope gradient-height scatter plot with Culmann and Newmark curves, (center) hillslope gradient-height density plot and histograms, (right) frequency-area plots of mapped (blue) and synthetic (green) landslide distributions.

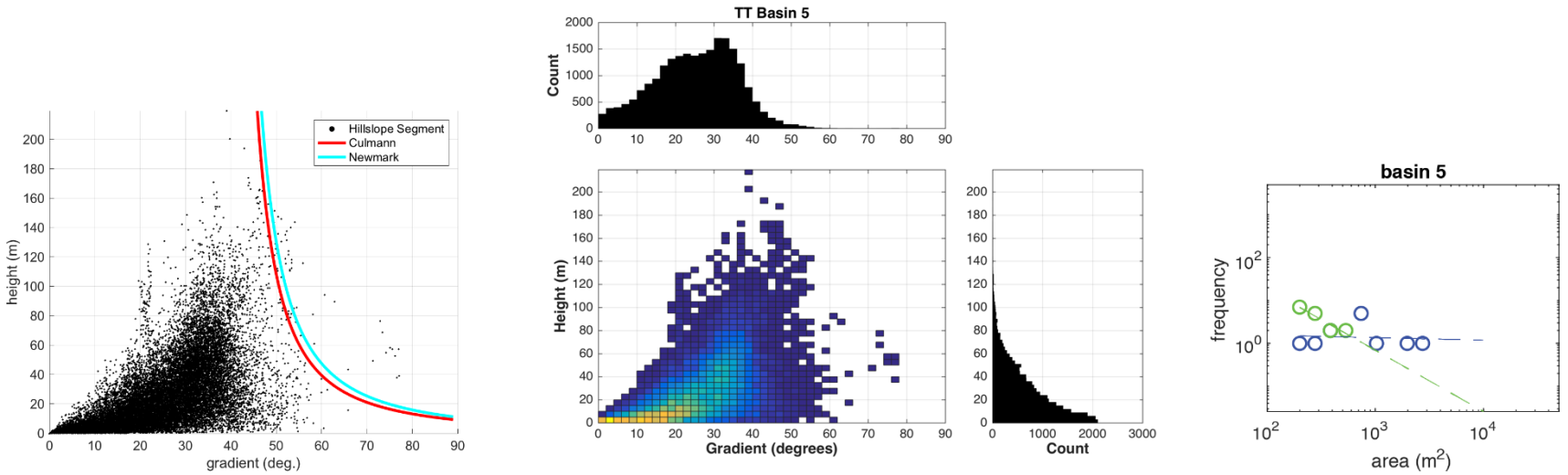

Figure S9. (left) Basin 5 hillslope gradient-height scatter plot with Culmann and Newmark curves, (center) hillslope gradient-height density plot and histograms, (right) frequency-area plots of mapped (blue) and synthetic (green) landslide distributions.

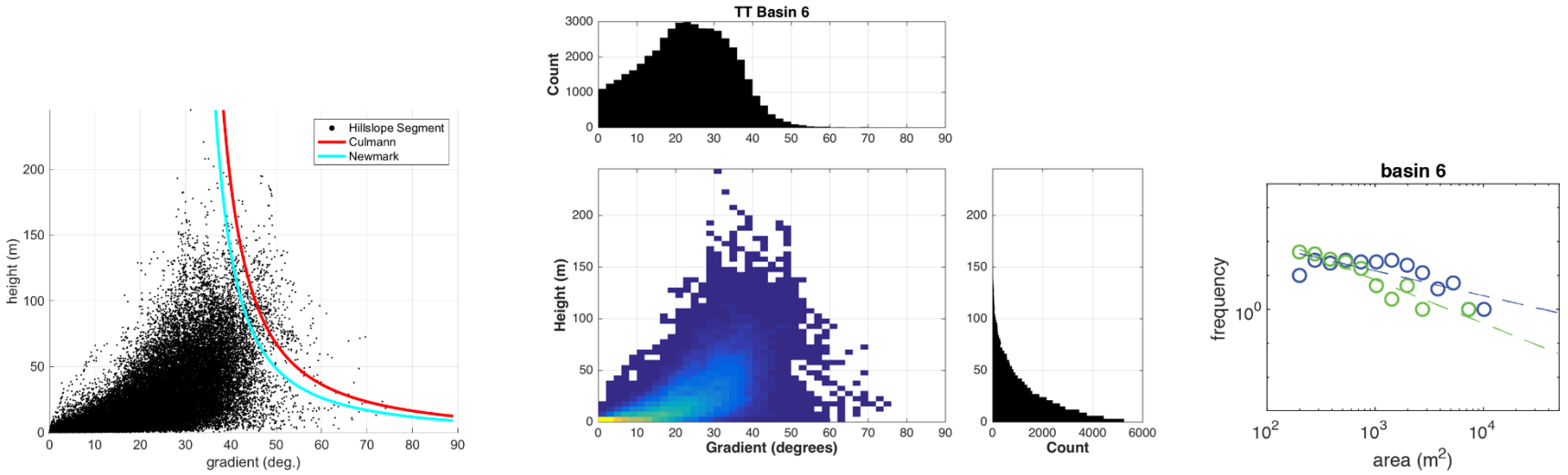

Figure S10. (left) Basin 6 hillslope gradient-height scatter plot with Culmann and Newmark curves, (center) hillslope gradient-height density plot and histograms, (right) frequency-area plots of mapped (blue) and synthetic (green) landslide distributions.

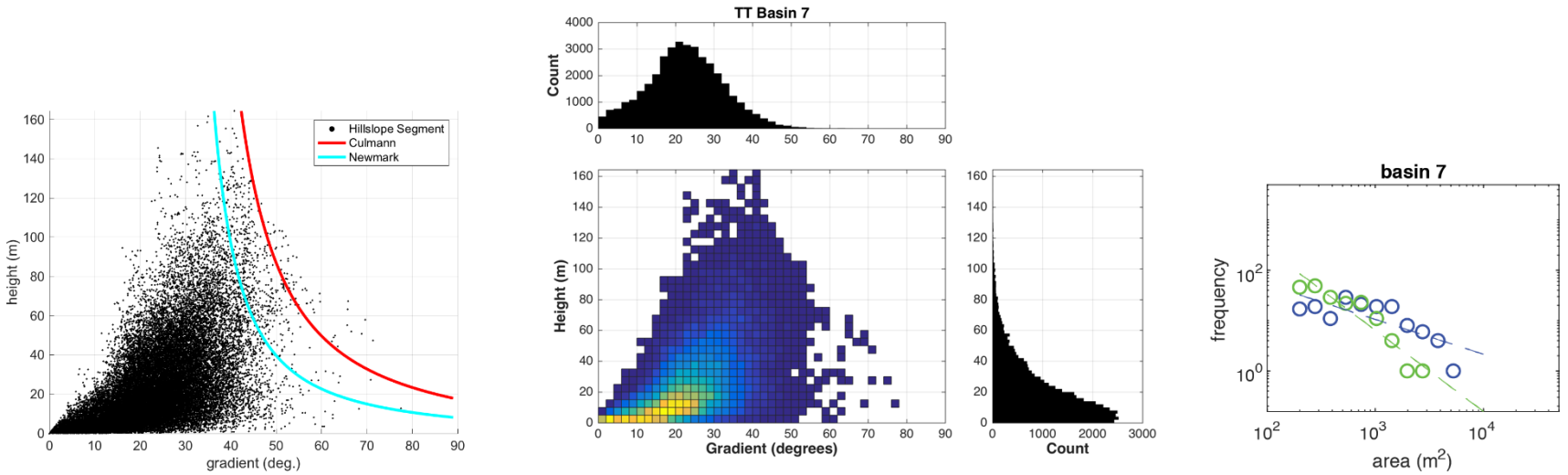

Figure S11. (left) Basin 7 hillslope gradient-height scatter plot with Culmann and Newmark curves, (center) hillslope gradient-height density plot and histograms, (right) frequency-area plots of mapped (blue) and synthetic (green) landslide distributions.

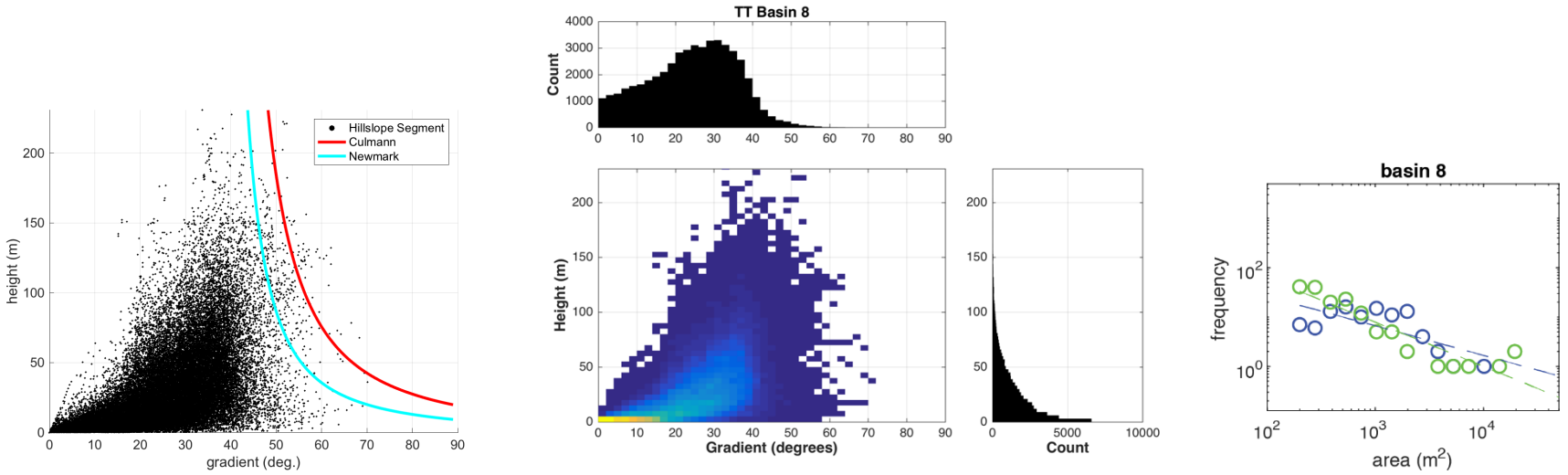

Figure S12. (left) Basin 8 hillslope gradient-height scatter plot with Culmann and Newmark curves, (center) hillslope gradient-height density plot and histograms, (right) frequency-area plots of mapped (blue) and synthetic (green) landslide distributions.

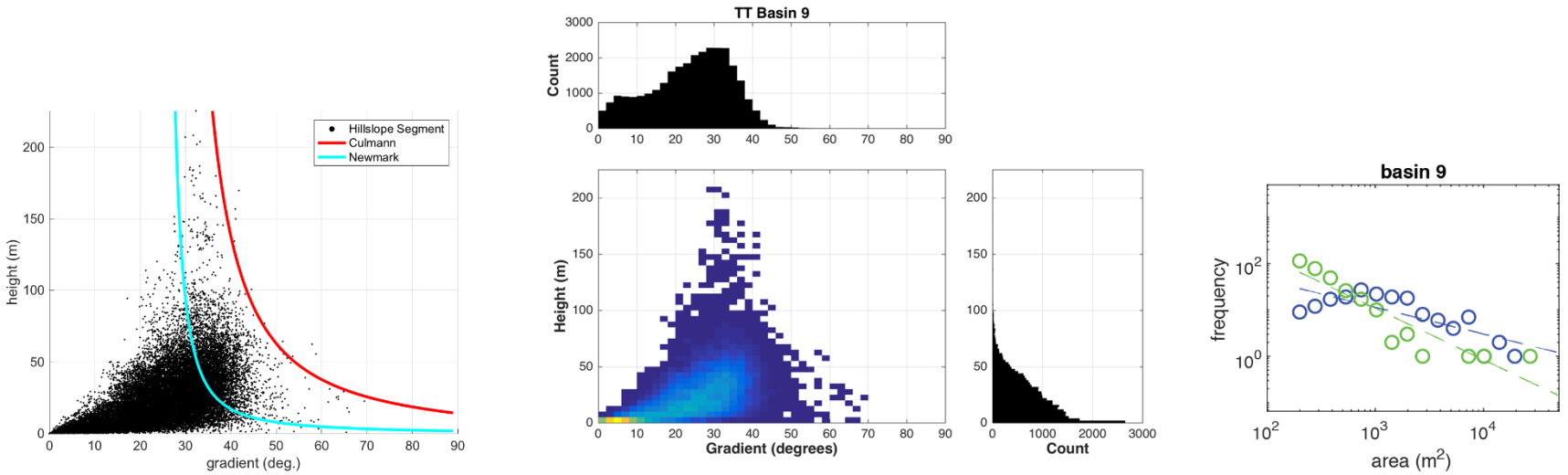

Figure S13. (left) Basin 9 hillslope gradient-height scatter plot with Culmann and Newmark curves, (center) hillslope gradient-height density plot and histograms, (right) frequency-area plots of mapped (blue) and synthetic (green) landslide distributions.

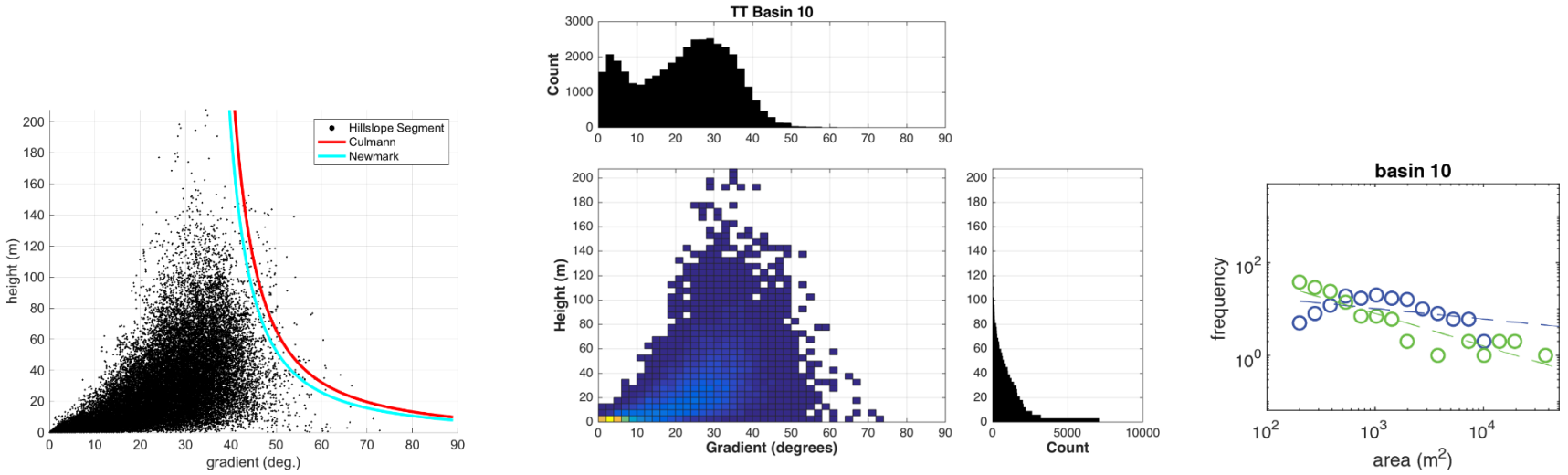

Figure S14. (left) Basin 10 hillslope gradient-height scatter plot with Culmann and Newmark curves, (center) hillslope gradient-height density plot and histograms, (right) frequency-area plots of mapped (blue) and synthetic (green) landslide distributions.

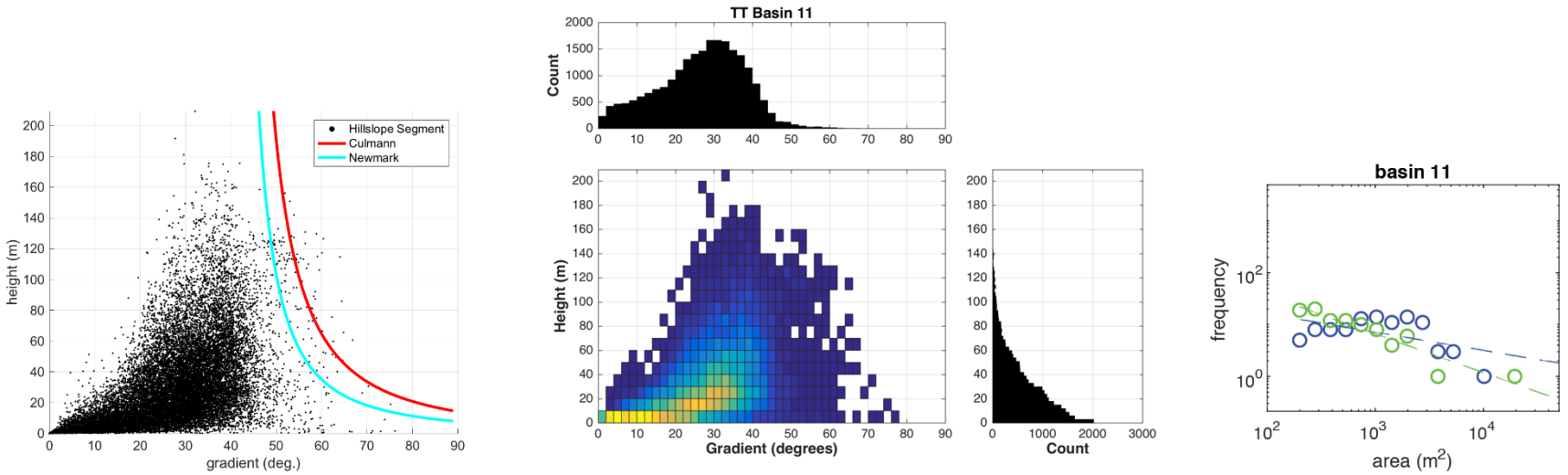

Figure S15. (left) Basin 11 hillslope gradient-height scatter plot with Culmann and Newmark curves, (center) hillslope gradient-height density plot and histograms, (right) frequency-area plots of mapped (blue) and synthetic (green) landslide distributions.

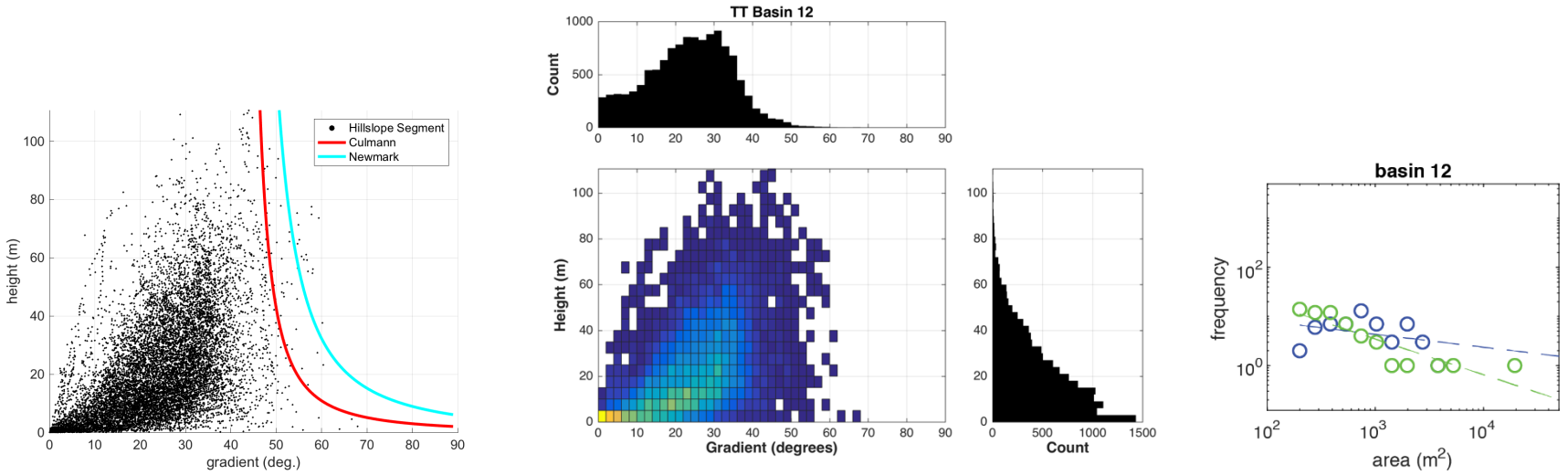

Figure S16. (left) Basin 12 hillslope gradient-height scatter plot with Culmann and Newmark curves, (center) hillslope gradient-height density plot and histograms, (right) frequency-area plots of mapped (blue) and synthetic (green) landslide distributions.

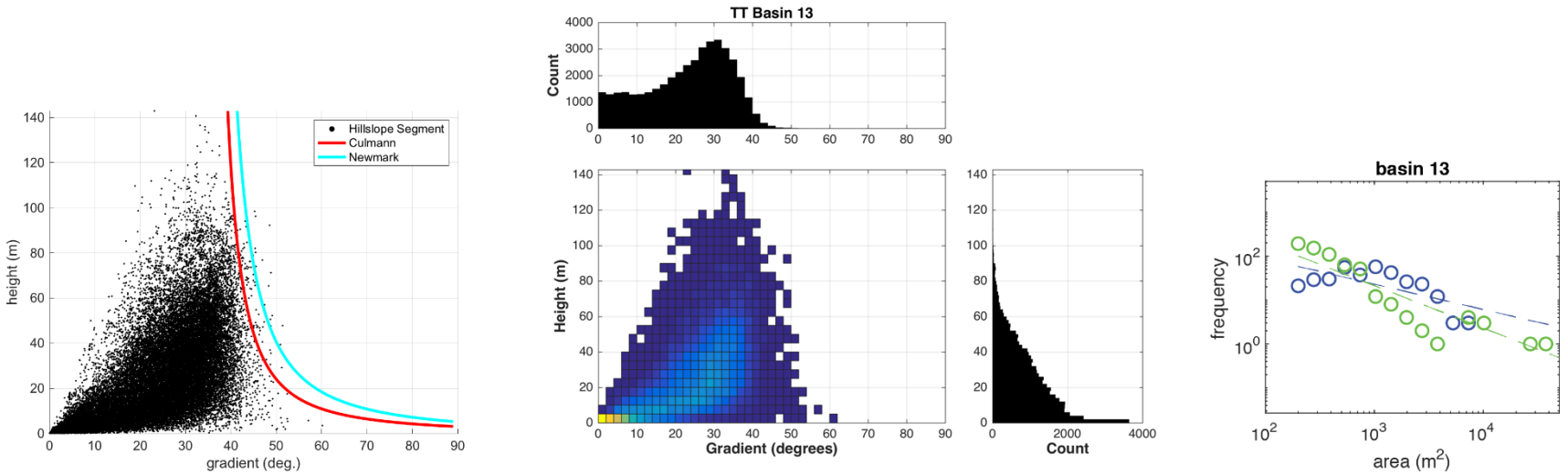

Figure S17. (left) Basin 13 hillslope gradient-height scatter plot with Culmann and Newmark curves, (center) hillslope gradient-height density plot and histograms, (right) frequency-area plots of mapped (blue) and synthetic (green) landslide distributions.

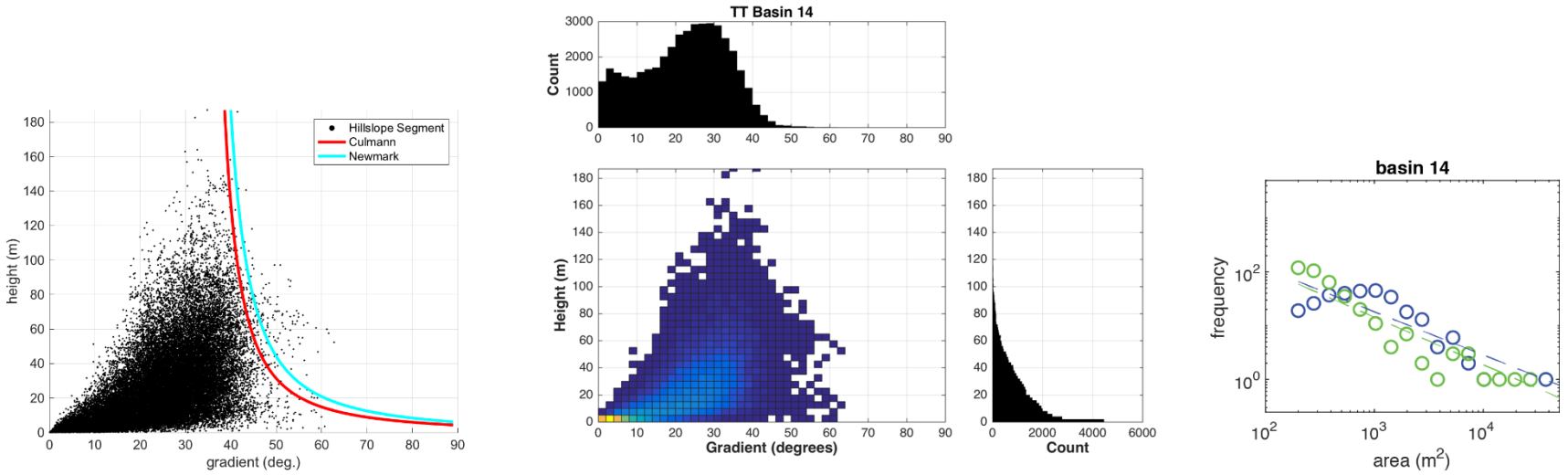

Figure S18. (left) Basin 14 hillslope gradient-height scatter plot with Culmann and Newmark curves, (center) hillslope gradient-height density plot and histograms, (right) frequency-area plots of mapped (blue) and synthetic (green) landslide distributions.

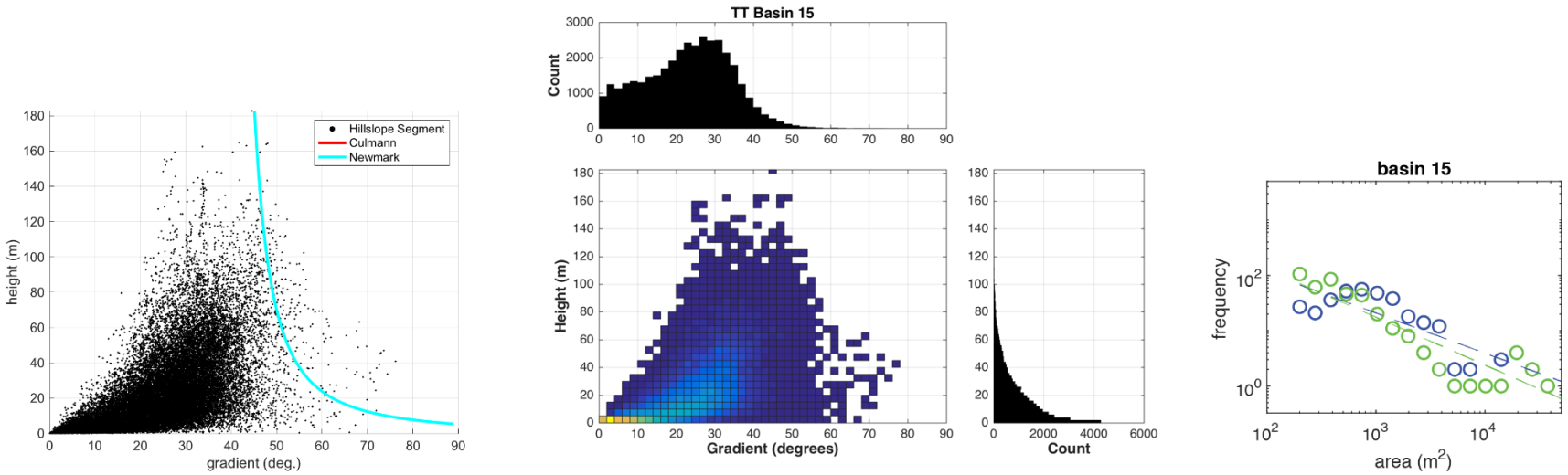

Figure S19. (left) Basin 15 hillslope gradient-height scatter plot with Culmann and Newmark curves, (center) hillslope gradient-height density plot and histograms, (right) frequency-area plots of mapped (blue) and synthetic (green) landslide distributions.

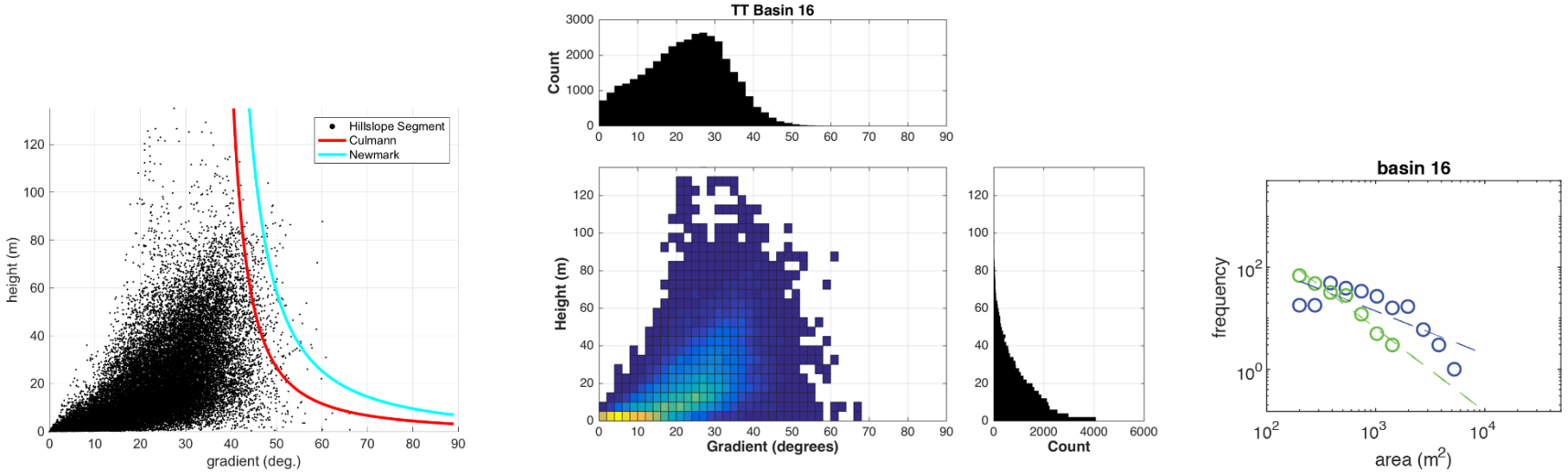

Figure S20. (left) Basin 16 hillslope gradient-height scatter plot with Culmann and Newmark curves, (center) hillslope gradient-height density plot and histograms, (right) frequency-area plots of mapped (blue) and synthetic (green) landslide distributions.

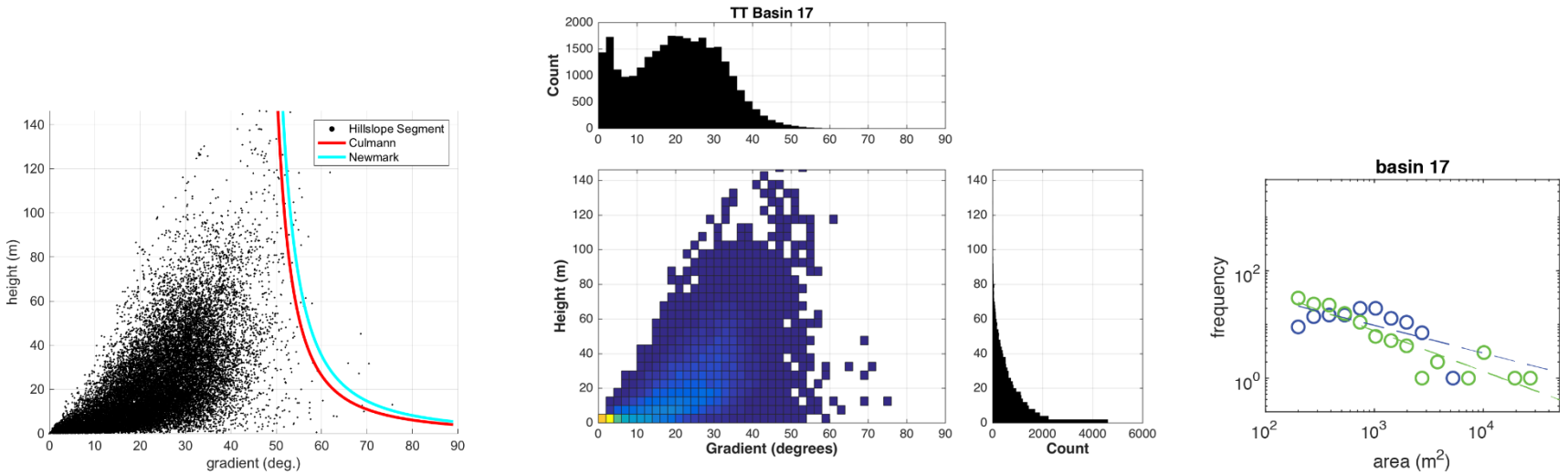

Figure S21. (left) Basin 17 hillslope gradient-height scatter plot with Culmann and Newmark curves, (center) hillslope gradient-height density plot and histograms, (right) frequency-area plots of mapped (blue) and synthetic (green) landslide distributions.

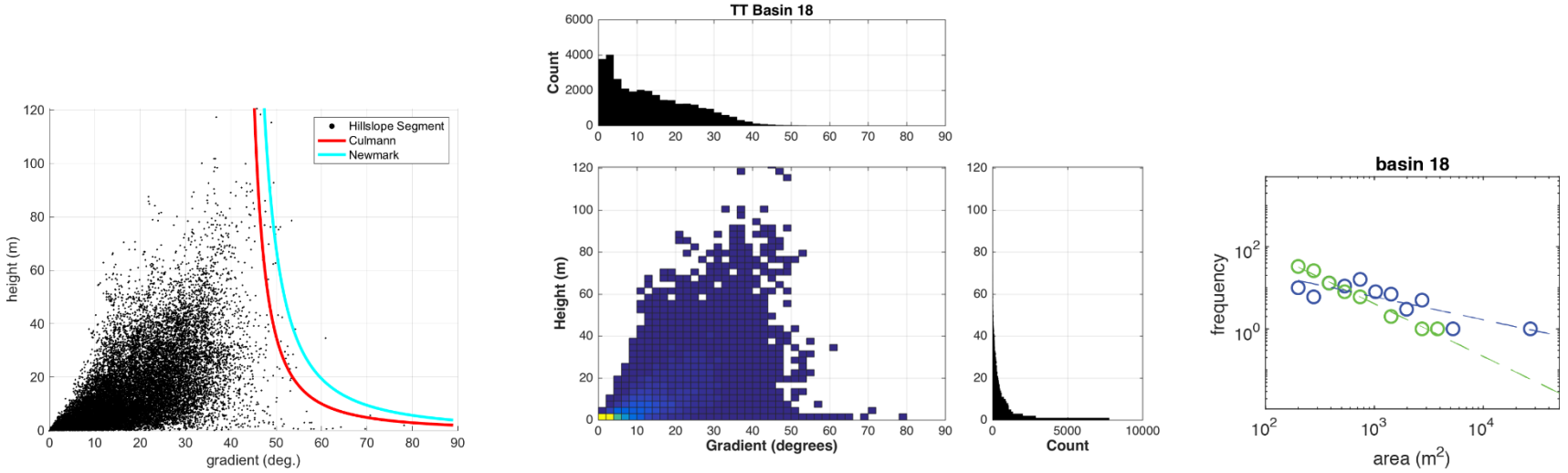

Figure S22. (left) Basin 18 hillslope gradient-height scatter plot with Culmann and Newmark curves, (center) hillslope gradient-height density plot and histograms, (right) frequency-area plots of mapped (blue) and synthetic (green) landslide distributions.

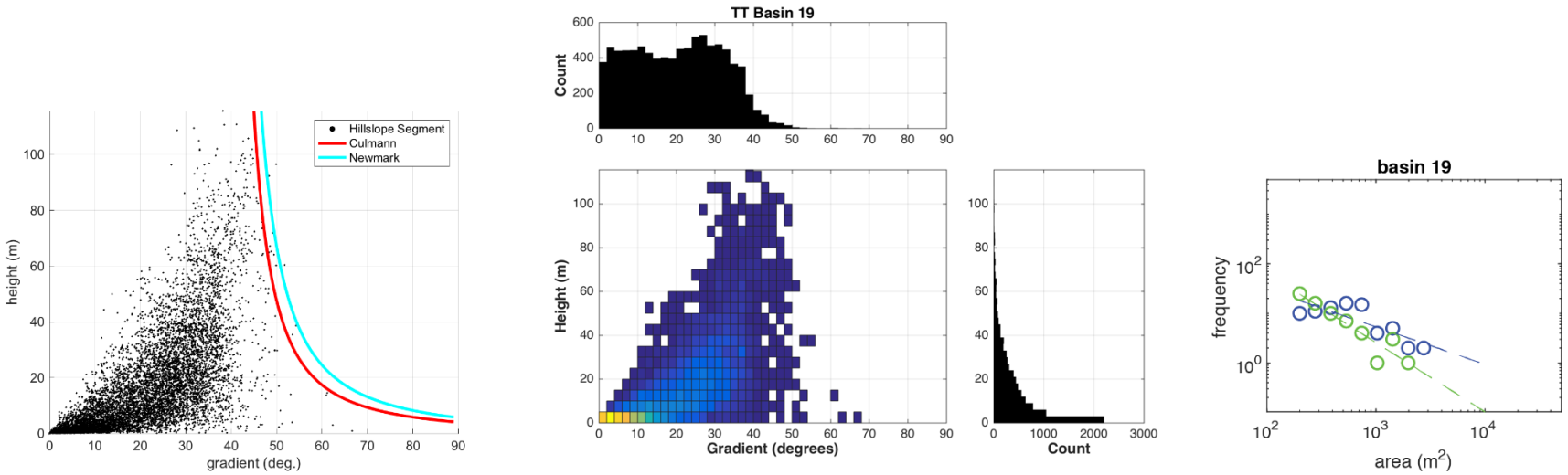

Figure S23. (left) Basin 19 hillslope gradient-height scatter plot with Culmann and Newmark curves, (center) hillslope gradient-height density plot and histograms, (right) frequency-area plots of mapped (blue) and synthetic (green) landslide distributions.

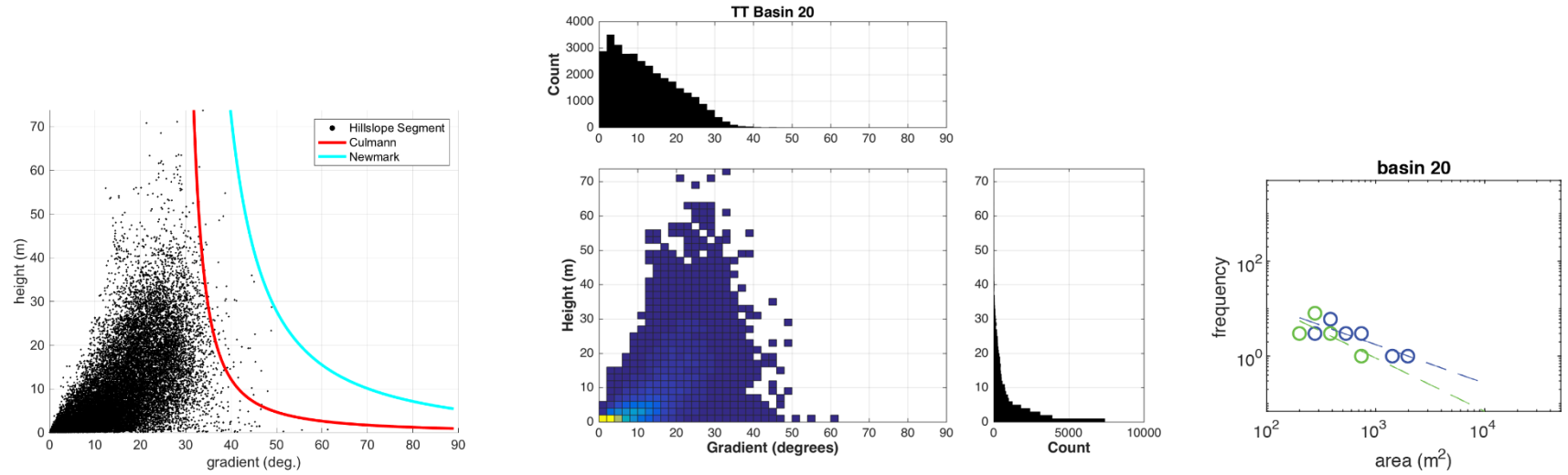

Figure S24. (left) Basin 20 hillslope gradient-height scatter plot with Culmann and Newmark curves, (center) hillslope gradient-height density plot and histograms, (right) frequency-area plots of mapped (blue) and synthetic (green) landslide distributions.

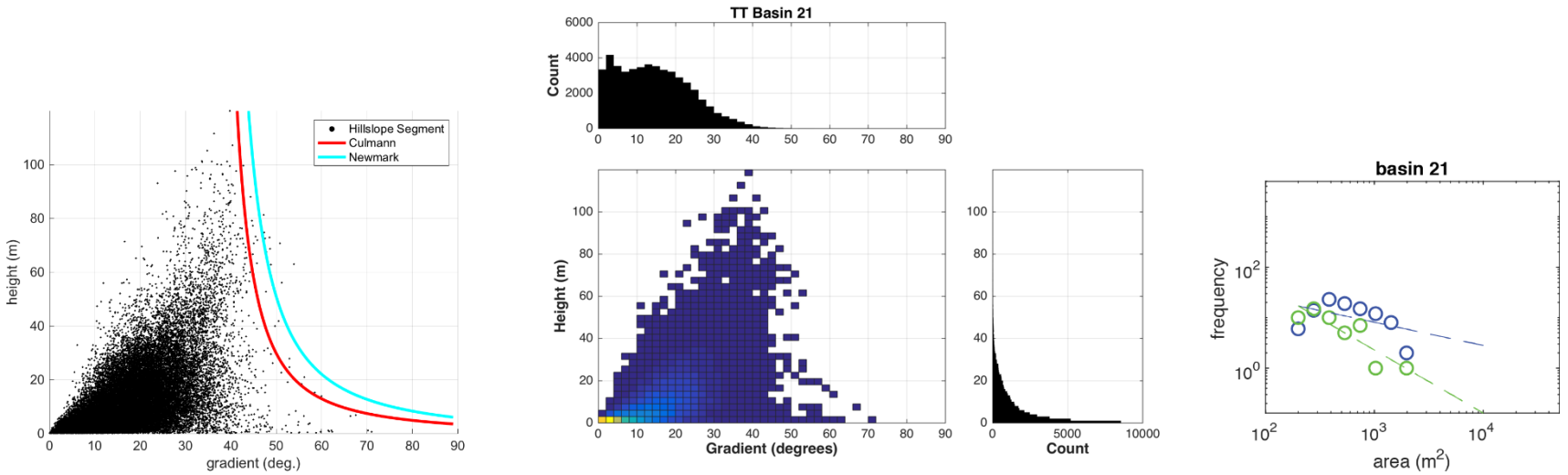

Figure S25. (left) Basin 21 hillslope gradient-height scatter plot with Culmann and Newmark curves, (center) hillslope gradient-height density plot and histograms, (right) frequency-area plots of mapped (blue) and synthetic (green) landslide distributions.

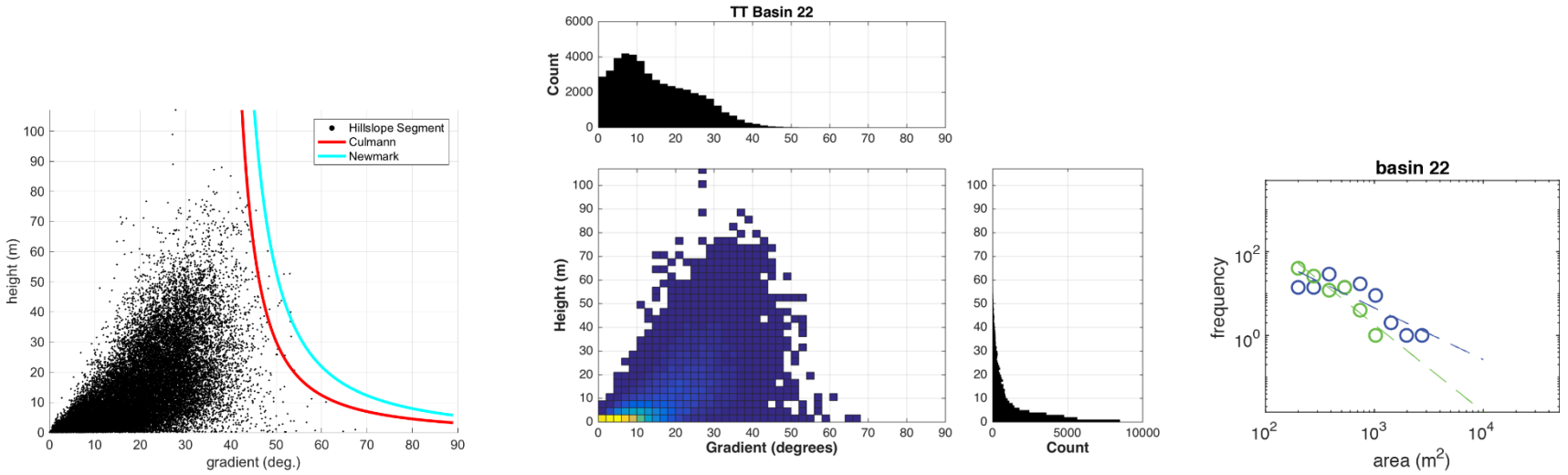

Figure S26. (left) Basin 22 hillslope gradient-height scatter plot with Culmann and Newmark curves, (center) hillslope gradient-height density plot and histograms, (right) frequency-area plots of mapped (blue) and synthetic (green) landslide distributions.

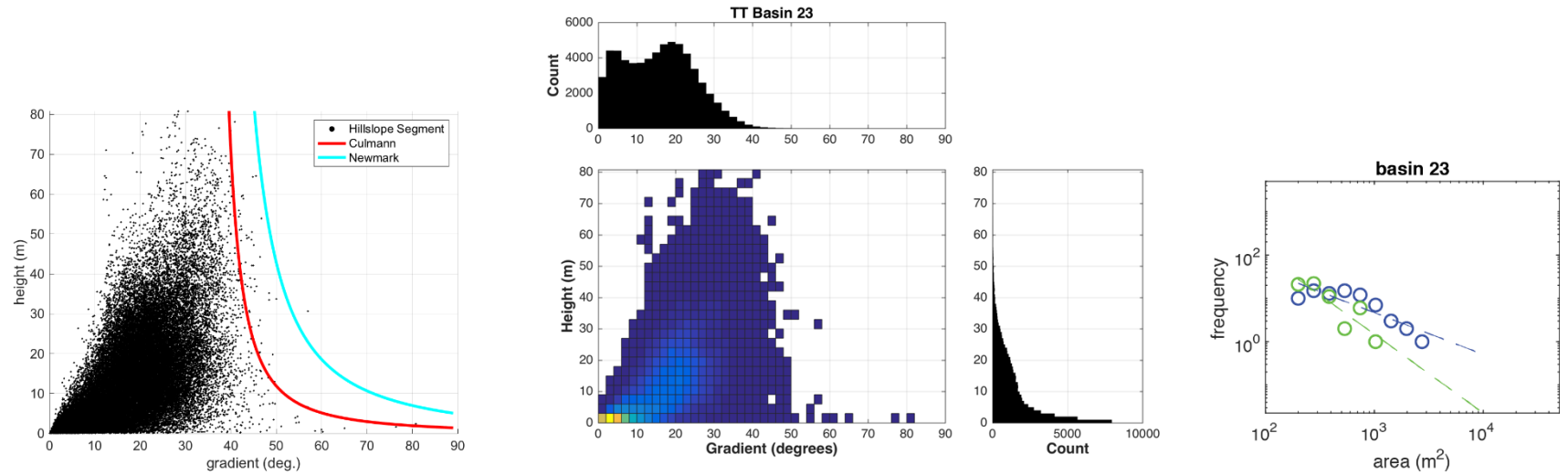

Figure S27. (left) Basin 23 hillslope gradient-height scatter plot with Culmann and Newmark curves, (center) hillslope gradient-height density plot and histograms, (right) frequency-area plots of mapped (blue) and synthetic (green) landslide distributions.

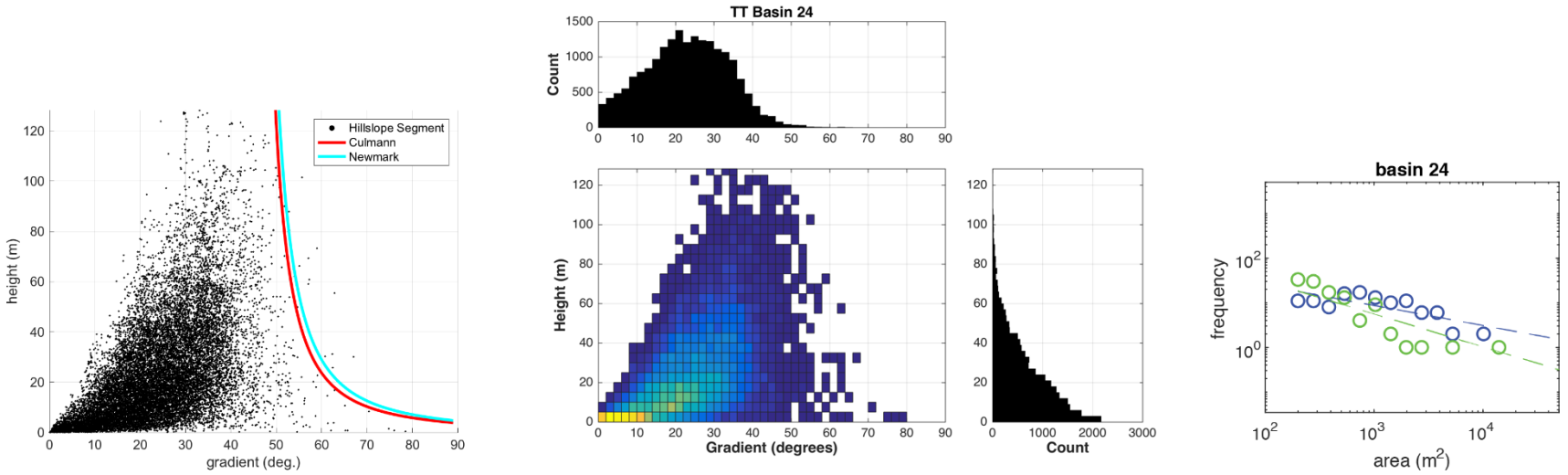

Figure S28. (left) Basin 24 hillslope gradient-height scatter plot with Culmann and Newmark curves, (center) hillslope gradient-height density plot and histograms, (right) frequency-area plots of mapped (blue) and synthetic (green) landslide distributions.

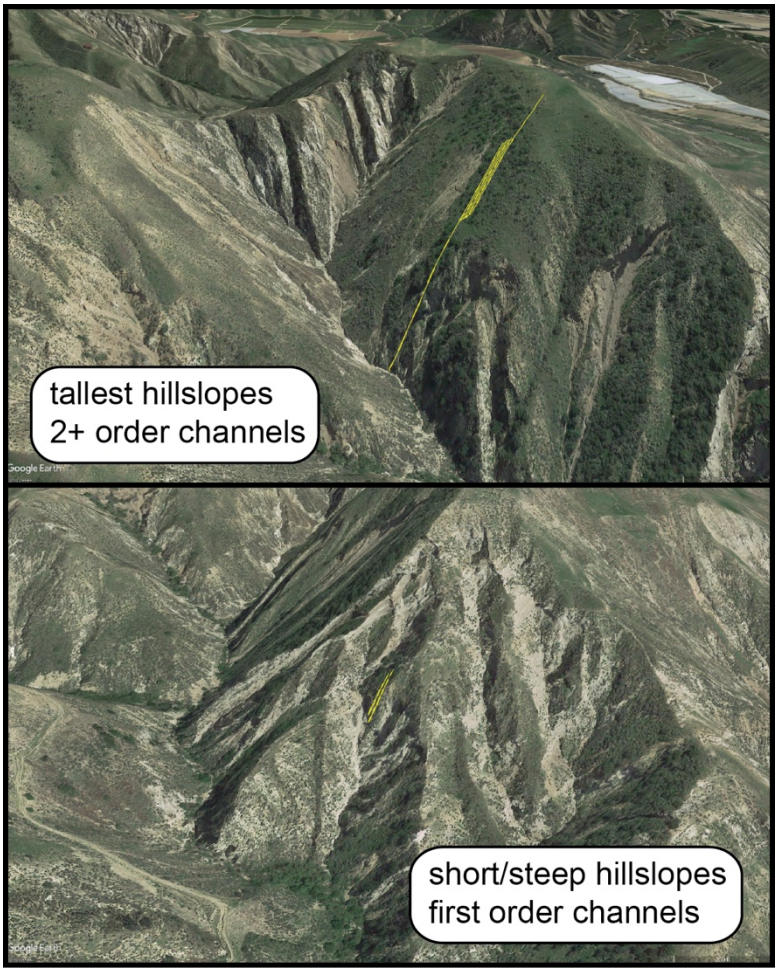

Figure S29. Example locations of hillslopes in Basin 1. The tallest threshold hillslopes are generally located above second order and greater channels, while short/steep threshold hillslopes are typically located above first-order channels.

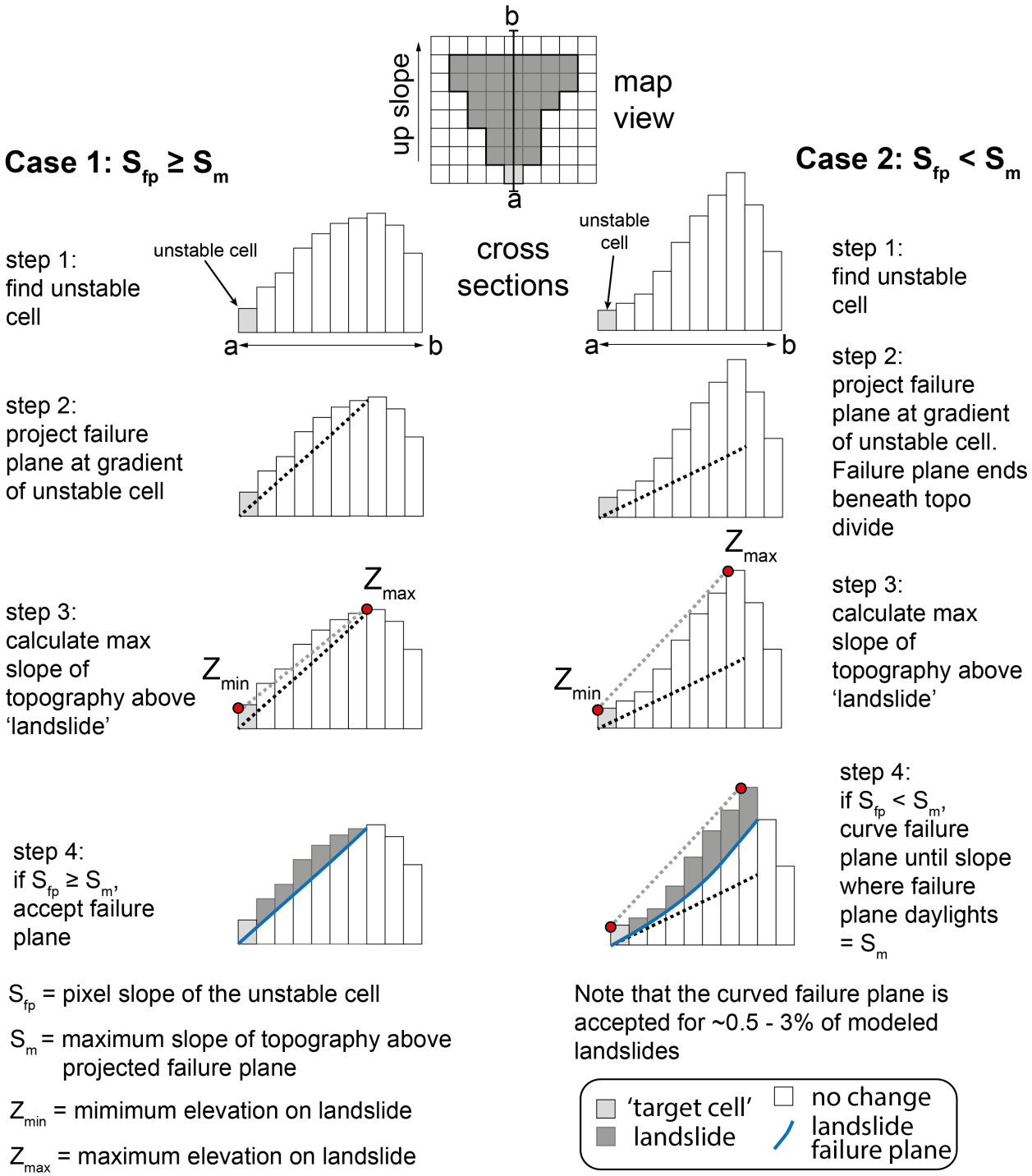

Figure S30. Generalized method used to find the landslide failure plane projected upslope from Newmark failure cells in a digital landscape.

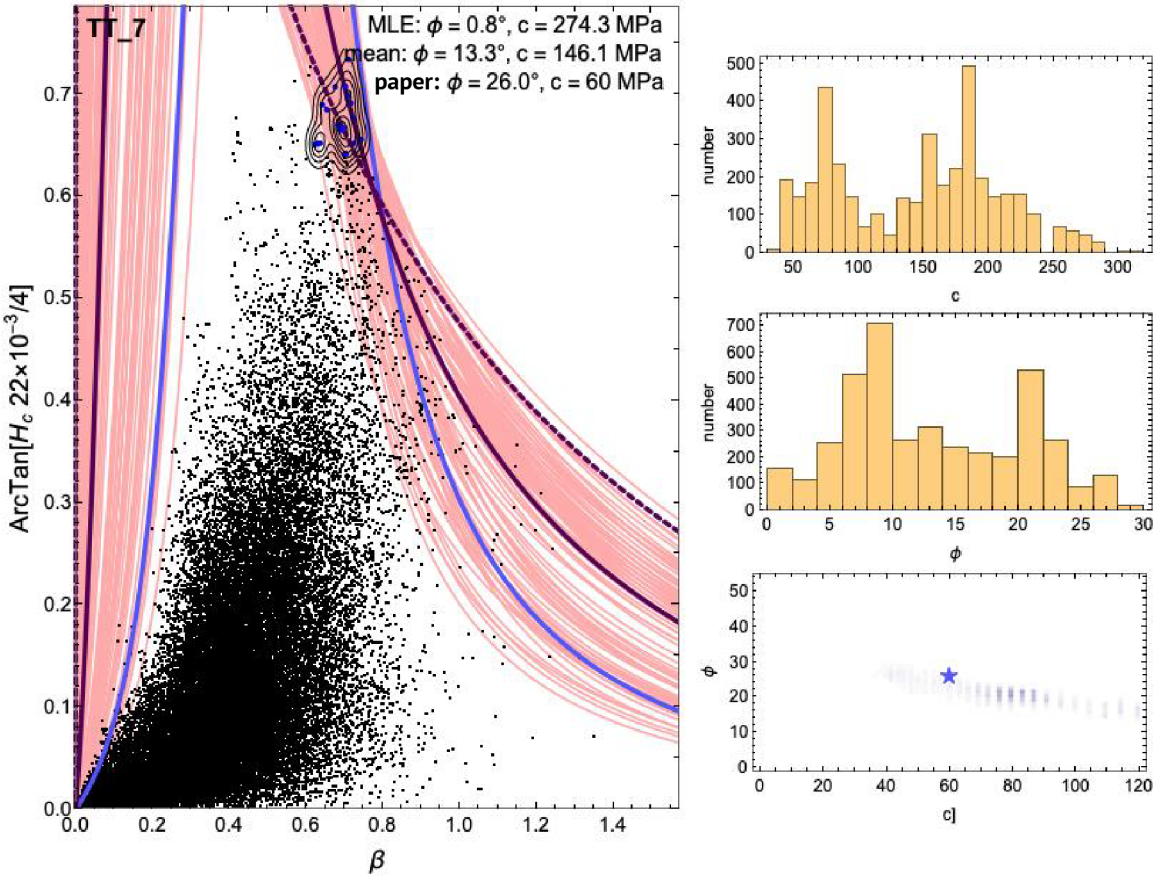

Figure S31. Example of an attempted quantitative approach to fitting the Culmann model to the threshold of scatter data, with hillslope data from basin 7. The MCMC approach requires models pass through the tallest/steepest hillslopes by assigning a prior probability based on the density of data above 99.9% quantile in height, and 50% quantile in gradient at those heights, shown by PDF contours in the scatter plot. The MLE, and mean of posteriors, produce lower friction angle estimates than is characteristic of most earth materials. Histograms of posteriors demonstrate wide range of cohesion and friction angle estimates.

Sample	Longitude (°W)	Latitude (°N)	Elevation (m)	Mean Age[1] (Ma)
16-PC-1	118.7612	34.46701	344	-- [2]
16-PC-3	118.7597	34.47153	347	-- [3]
16-PC-4	118.7557	34.46217	365	3.9 ± 1.2

[1] Mean age includes 2-sigma standard error
[2] One-sigma standard deviation of bedrock replicate analyses after outlier removal is greater than 45 percent of mean age. No mean age is reported.
[3] Replicate ages are older than the depositional age of the formation, indicating that ages are inherited and do not reflect cooling of the host rock. No mean age is reported.

Table S1. Sample locations and mean apatite (U-Th)/He ages. Sample locations are also shown in Figures 1 and S1.

Name	U ppm (ppm)	U SD (ppm)	Th (ppm)	Th SD (ppm)	Sm (ppm)	Sm SD (ppm)	He (ncc)	He error (ncc)	He (ncc/g)	Shape[1]	Effective Uranium (eU) (ppm)	Mass (mg)	FT[2]	Radius (um)	Length (um)	Uncorrected Age	Corrected Age (Ma)	Age Error[3]
16-PC-01a	12.35	0.18	27.40	0.43	31.24	0.50	0.0343	0.00022	14991.093	pp	18.92	0.0023	0.76	56.3	89.7	6.2	8.07	0.08
16-PC-01b	20.11	0.29	41.40	0.60	331.25	5.04	0.0173	0.00016	13918.051	nn	31.45	0.0012	0.70	40.4	94.6	3.3	4.79	0.05
16-PC-01c	39.27	0.56	41.07	0.59	240.54	3.59	0.2930	0.00058	110617.591	np	50.09	0.0026	0.76	51.0	126.4	18.4	24.26	0.22
16-PC-01d	7.96	0.12	11.02	0.16	34.38	0.58	0.0276	0.00009	11498.488	np	10.71	0.0024	0.75	49.3	122.8	8.3	11.02	0.10
16-PC-03a	27.47	0.39	32.34	0.47	54.62	0.89	0.1572	0.00025	65222.872	np	35.31	0.0024	0.74	44.8	148.8	15.1	20.50	0.18
16-PC-03b†	3.47	0.06	12.77	0.20	97.36	1.52	0.0380	0.00013	18432.188	pp	6.94	0.0021	0.71	40.2	158.1	21.8	30.47	0.25
16-PC-03c	8.25	0.12	23.92	0.34	92.03	1.43	0.0735	0.00017	31206.602	np	14.31	0.0024	0.74	47.0	132.1	17.9	23.99	0.19
16-PC-03d	19.57	0.28	11.95	0.17	220.10	3.24	0.2668	0.00054	99839.500	pp	23.47	0.0027	0.74	45.1	163.4	36.1	48.68	0.46
16-PC-04a‡	42.26	0.61	36.85	0.56	98.16	1.47	0.1284	0.00050	118772.223	pp	51.37	0.0011	0.70	43.3	71.6	18.9	27.04	0.24
16-PC-04b	11.87	0.17	15.78	0.23	25.25	0.48	0.0095	0.00012	4924.689	pp	15.69	0.0019	0.72	41.1	141.3	2.0	2.83	0.03
16-PC-04d	15.67	0.23	14.31	0.21	23.41	0.43	0.0210	0.00014	7714.107	np	19.14	0.0027	0.76	49.5	138.3	3.0	3.98	0.04
16-PC-04e	17.19	0.25	13.90	0.20	49.08	0.73	0.0468	0.00025	10146.815	nn	20.67	0.0046	0.80	59.6	161.2	3.9	4.91	0.05

† Age excluded from calculation of mean age due to and standard error due to low Uranium content (<5ppm).
‡ Age identified as an outlier by the statistical test of Dean and Dixon (1951) at the 90 percent confidence interval and excluded from calculation of mean age and standard error.
[1] The Following terms refer to the morphology of apatite grains: nn = a grain with two unbroken euhedral tips; pp = a grain with both tips broken such that they are roughly perpendicular to the c-axis; np = a grain with one unbroken tip and one tip broken roughly perpendicular to the c-axis; multigrain = multiple apatite grains degassed for 4He within one packet due to low single-grain 4He yield.
[2] Ft is alpha-ejection correction after Farley et al., (1996).
[3] The age error reported for single grained ages represents the propagated one-sigma uncertainty based on the analytical error in measuring He, U, Th and Sm.

Table S2. Single-grain apatite (U-Th-Sm)/He analyses.

Basin #	Culmann C (kPa)	Culmann Phi (deg.)	Newmark C[1] (kPa)	Newmark C/t[2] (kPa/m)	Basin Area (km^2)	Max Hillslope Height (m)	Mean Hillslope Height (m)	Max Pixel Slope (deg.)	Mean Pixel Slope (deg.)	STD Pixel Slope (deg.)	Landslide Count	Average Newmark Landslide Thickness (m)	Average Culmann Landslide Thickness[3] (m)	Average Threshold Landslide Thickness[4] (m)	Geologic Unit[5]
1	21	33	22.2	10.2	12.0	233.8	29.5	75.0	28.6	12.3	451	2.6	1.9	3.8	Tm
2	41	29	26.3	12.1	12.5	261.5	33.5	78.6	29.8	12.0	341	3.0	2.7	6.7	Tm
3	60	31	26.8	12.3	12.1	207.4	33.2	81.7	30.7	11.1	134	3.1	2.2	8.7	Tm
4	17	30	23.9	11.0	10.8	206.2	22.1	76.5	24.3	10.2	73	2.4	1.6	3.2	Tm
5	25	37	30.1	13.9	5.5	219.3	27.3	81.4	28.5	11.4	12	8.2	1.4	4.3	Tm
6	40	28	28.9	13.3	10.9	245	26.8	84.4	27.7	11.4	230	3.8	2.5	6.5	Tm
7	60	26	27.4	12.6	8.5	164.3	23.1	77.8	25.5	10.5	168	3.2	2.1	8.3	Tm
8	55	35	25.9	11.9	12.2	230.7	28.6	81.8	27.8	12.1	106	5.3	1.8	8.1	Tm
9	50	24	6.2	2.86	6.5	225.2	23.5	70.6	25.9	11.1	182	1.8	2.1	7.7	Tp
10	30	31	24.0	11.0	9.6	207.5	25.4	72.4	25.2	11.9	158	3.0	1.7	5.0	Tp
11	38	38	20.6	9.5	5.7	209.4	30.5	79.9	28.8	11.7	105	6.4	1.4	6.0	Tm
12	5	41	14.8	6.8	3.0	110.6	21.5	72.2	23.2	13.1	59	3.1	1.1	1.0	Tp
13	9	33	15.2	7.0	9.6	135.7	24.6	66.9	24.7	11.4	378	1.6	1.0	1.7	Tp
14	13	32	18.3	8.4	10.5	165.2	24.9	72.2	25.0	11.1	309	2.0	1.3	2.5	Tp
15	14	38	14.0	6.4	8.1	164	22.5	78.4	26.2	11.7	362	2.7	1.3	2.6	Tp
16	9	34	19.6	9.0	7.8	131.6	19.8	72.5	24.7	11.4	254	2.8	1.1	1.7	Tp
17	9	44	12.1	5.6	6.2	146.4	19.9	76.9	23.5	12.1	141	3.4	1.3	1.7	Tp
18	5	40	9.7	4.5	6.3	120.6	10.7	73.3	15.8	11.5	94	2.1	0.8	1.0	QTs
19	11	37	15.5	7.1	1.8	115.6	16.7	69.9	23.8	12.7	90	1.9	1.1	2.0	Tp
20	3	27	17.8	8.2	5.5	73.8	7.4	59.1	13.8	9.6	20	1.8	0.5	0.6	QTs
21	10	34	17.1	7.9	9.0	119.9	9.8	75.7	16.8	10.3	108	2.1	0.8	1.8	QTs
22	9	35	15.9	7.3	8.3	107	9.6	70.1	17.7	11.4	117	2.2	0.7	1.7	QTs
23	4	34	14.4	6.6	12.4	80.8	11.7	60.0	17.6	9.5	94	1.7	0.6	0.8	QTs
24	9	43	11.0	5.1	4.6	128.2	23	75.1	24.5	11.6	125	2.8	0.9	1.7	Tp

[1] Calculated with Phi equal to the Culmann phi estimate
[2] Cohesion/(landslide thickness) model results. Values are multiplied by the median landslide thickness to produce estimates of cohesion in kPa.
[3] Culmann model estimates of landslide thickness were calculated using each hillslope gradient-height pair in a basin. Landslide failure angle is calculated as the geometric mean of the friction angle and hillslope gradient, i.e. $\theta = (\phi + \beta)/2$ (Lu and Godt, 2013). Thickness is calculated as the mean height of the resultant wedge, measured normal to the landslide failure plane.
[4] Threshold model estimates of landslide thickness were calculated with gradient-hillslope pairs that fall on the Culmann curve set by C and ϕ, in increments of 0.1 degrees. Landslide failure angle is calculated as the geometric mean of the friction angle and hillslope gradient, i.e. $\theta = (\phi + \beta)/2$ (Lu & Godt, 2013). Thickness is calculated as the mean height of the resultant wedge, measured normal to the landslide failure plane.
[5] Predominant geologic unit within each basin area. Tm = Monterey Formation, Tp = Pico Formation, and QTs = Saugus Formation. From Dibblee (1991, 1993) and Dibblee and Ehrenspeck (1996, 1997).

Table S3. Basin-averaged strength and topographic measurements.

Basin #	Minimum Burial Depth (m)	Maximum Burial Depth (m)	Average Burial Depth (m)
1	3300	4000	3600
2	3300	4500	3900
3	4000	5300	4700
4	3300	4300	3800
5	4300	4800	4500
6	3300	4800	4000
7	4100	4900	4500
8	4100	4900	4500
9	1900	2900	2400
10	2900	3300	3100
11	3300	4200	3800
12	2900	3300	3100
13	2100	3000	2500
14	2100	3500	2800
15	1900	3300	2600
16	2100	3300	2700
17	2900	3500	3200
18	0	2200	1100
19	2100	2600	2300
20	500	2300	1400
21	1000	2200	1600
22	500	2100	1300
23	1300	2100	1700
24	2100	3300	2700

Table S4. Burial depth of sedimentary rocks by basin.